INTERNATIONAL JOURNAL FOR NUMERICAL METHODS IN FLUIDS
Int. J. Numer. Meth. Fluids 2011; **00**:1–31
Published online in Wiley InterScience (www.interscience.wiley.com). DOI: 10.1002/fld

Shape optimization for viscous flows by reduced basis methods and free-form deformation

Andrea Manzoni[1], Alfio Quarteroni[1,2], Gianluigi Rozza[1,*,†]

[1]*CMCS - Modelling and Scientific Computing, MATHICSE - Mathematics Institute of Computational Science and Engineering, EPFL - Ecole Polytechnique Fédérale de Lausanne, Station 8, CH-1015 Lausanne, Switzerland.*
[2]*MOX - Modellistica e Calcolo Scientifico, Dipartimento di Matematica "F. Brioschi', Politecnico di Milano, P.za Leonardo da Vinci 32, I-20133 Milano, Italy.*

SUMMARY

In this paper we further develop an approach previosuly introduced in [23] for shape optimization that combines a suitable low-dimensional parametrization of the geometry (yielding a geometrical reduction) with reduced basis methods (yielding a reduction of computational complexity). More precisely, free-form deformation techniques are considered for the geometry description and its parametrization, while reduced basis methods are used upon a finite element discretization to solve systems of parametrized partial differential equations. This allows an efficient flow field computation and cost functional evaluation during the iterative optimization procedure, resulting in effective computational savings with respect to usual shape optimization strategies. This approach is very general and can be applied to a broad variety of problems. In this paper we apply it to find the optimal shape of aorto-coronaric bypass anastomoses based on vorticity minimization in the down-field region. Blood flows in the coronary arteries are modelled using Stokes equations; afterwards, results have been verified in feedback using Navier-Stokes equations. Copyright © 2011 John Wiley & Sons, Ltd.

Received . . .

KEY WORDS: Model order reduction; reduced basis methods; free-form deformation; shape optimization; haemodynamics; Stokes equations

1. INTRODUCTION AND MOTIVATION

The efficient solution of optimal control or shape optimization problems involving partial differential equations (PDEs) is a problem of interest for computational scientists in many applicative contexts. The goal is the minimization/maximization of a given cost functional under constraints (algebraic, topological or differential), the control being represented by either suitable variables (such as sources, model coefficients or boundary values) or the shape of the domain itself.

[†]E-mail: gianluigi.rozza@epfl.ch
[*]Correspondence to: Gianluigi Rozza, CMCS - Modelling and Scientific Computing, MATHICSE - Mathematics Institute of Computational Science and Engineering, EPFL - Ecole Polytechnique Fédérale de Lausanne, Station 8, CH-1015 Lausanne, Switzerland.

In this paper we focus on the latter class of problems referred as *shape optimization* or *optimal shape design* problems [2, 18, 24, 27]. In fluid mechanics, cost functionals are expressed in terms of flow variables (such as velocity, pressure, temperature, etc.), while constraints are represented by the PDE (advection-diffusion, Stokes or Navier-Stokes equations, etc.) describing the flow, and by topological constraints on the shape of the domain, whenever necessary. In a broad variety of applications the design of devices able to reduce drag forces, dissipations or stresses greatly enhances the efficiency of a system. The reduction of drag in transportation vehicles (aircrafts, watercrafts) and of vorticity and stresses in biomedical devices, and the compliance minimization in cantilevers or membranes, represent further instances in which shape optimization techniques are called into play.

For the numerical solution of these problems, efficient procedures are required since *(i)* PDEs are expensive to solve when solutions need to capture fine details (such as velocity and thermal boundary layers, vorticity structures, etc.); *(ii)* the finite element assembling discretization procedures result expensive when problem geometry keeps changing; *(iii)* optimization requires recursive evaluations of the cost functional. For example, a classical shape optimization algorithm based on explicit boundary displacement can provide accurate solutions at the expence of being very unefficient since at each step PDEs have to be solved for a new geometrical configuration. A key to simplification consists of making use of a reference configuration on which every problem is brought back and solved at each iteration of the optimization process, and geometry variations are accounted for the equation coefficients.

The introduction of a suitable (low-dimensional) shape parametrization is thus instrumental to reduce both the geometrical and computational complexity. Obviously, shape parametrization has to be flexible enough to describe a wide family of admissible shapes without substantially increasing the number of parameters and, at the same time, it should be computationally efficient to allow for a fast solution of the parametrized PDEs. Free-form deformation (FFD) techniques [3, 7, 42] provide a powerful tool for representing global and smooth deformations acting on a small number of design parameters. Once the shape has been parametrized, we solve iteratively a partial differential (state) equation and evaluate the cost functional we want to minimize on the parametric domain. To do this, we rely on reduced basis (RB) methods for parametrized partial differential equations (P^2DEs) (see the review papers [31, 37]). Thanks to a suitable computational *Offline-Online* decomposition (see Sec. 5), RB methods provide rapid and reliable results at a greatly reduced cost, and are well-indicated above all in real-time (e.g. parameter estimation) and multi-query (e.g. optimization, control) contexts. The combination of FFD techniques with RB methods previously considered in [23, 38] allows a considerable geometrical saving (because of the low number of design parameters) as well as computational reduction (thanks to the reduced dimension of the linear system associated to the resulting discretized problems).

Let us recall the proposed approach to parametric shape optimization. First we introduce the mathematical formulation for parametric PDEs problems. Then, a suitable parametrization of the geometry is obtained by using free-form deformation (FFD): this technique allows to build a parametric map through which we reformulate our original problem on a reference configuration, resulting in a parametrized problem where the effect of geometry variations is traced back onto

DOI: 10.1002/fld

its parametrized transformation tensors. Since FFD techniques lead (in general) to non-affinely parametrized transformations of the computational domain, we approximate their components by means of affinely parametrized tensors, through the empirical interpolation method (EIM) [4]. In this way, we can perform a suitable Offline-Online computational strategy, through which reduced basis approximation gives a rapid and reliable field solution and cost functional evaluation. At the outer level, this is used in a suitable iterative procedure for the (now, parametric) optimization. This combined approach is rather general and can be used in a broad variety of applications. To provide a proof of its efficacy, in this paper we apply it to the design of cardiovascular prostheses in biological flows. More specifically, the design of a bypass graft has been formulated as a shape optimization and flow control problem in [33] and later studied using small perturbation techniques and asymptotic developments in Agoshkov et al. [1]. The RB framework applied to the Stokes problem approximation has been used to study a simple bypass design problem in presence of either affine or nonaffine shape parametrization, treating some shape geometrical dimensions as design parameters (see [34, 35, 40]).

In this paper we aim at extending this framework [23,38] by considering more complex applications, geometrical configurations and viscous equations (still not addressed in the mentioned references). Not only, we show how to handle more general shape parametrizations in order to either *(i)* enrich the family of possible shape configurations, and *(ii)* combine the RB framework with less *ad-hoc* tools for an efficient shape treatment, where (possibly) the parametric shape deformations result independent of the problem geometry, the flow model and the computational mesh. The approach we propose is in fact based on the coupling of three different tools – free-form deformation, empirical interpolation and reduced basis methods – and applied to steady incompressible Stokes equations. After the shape optimization procedure is carried out, an "a posteriori" high-fidelity feedback using Navier-Stokes equations is provided.

This combined "RB+FFD" approach features several advantages: it is very flexible, it involves the solution of low dimensional problems (with low geometrical dimension), yielding substantial computational savings without sacrificing numerical accuracy, even when addressing complex shape optimization problems. Needless to say, techniques and methods discussed in this work prove to be useful also in facing other optimization problems arising in haemodynamics and, more generally, in computational fluid dynamics.

The paper is organized as follows. In Sec. 2 we address an abstract formulation of our proposed reduction strategies for shape optimization problems. Then we recall the optimal bypass design problem in Sec. 3, providing a quick review of some bio-engineering aspects in Appendix A. In Sec. 4 and Sec. 5 we introduce the two ingredients standing at the basis of our reduction strategy, i.e. free-form deformation techniques for shape parametrization and reduced basis methods for flow simulation. In Sec. 6 we present our numerical procedure; then, we present in Sec. 7 some numerical results, address a brief comparison with results from literature and propose a feedback procedure. In the last Sec. 8 we sketch some possible future developments and improvements.

DOI: 10.1002/fld

2. MODEL ORDER REDUCTION FOR SHAPE OPTIMIZATION

The motivation inspiring this paper is the optimal design of a biological bypass (e.g. a coronary bypass). In this context, one should ideally aim at *(i) real-time* (since we could be interested in a very rapid solution) and a *(ii) many-query* (because of repetitive evaluations of different configurations) context. In this scenario, suitable parametrization techniques and RB methods allow to substantially enhance the method efficiency. Although in this paper we will not address the whole complexity hindered by such a challenging problem, yet we set up a mathematical approach that is apt at facing (simplified) problems of the same nature.

2.1. A general reduced framework for shape optimization

From an abstract point of view, shape optimization problems can be written as the minimization, over a set of admissible shapes $\mathcal{O}_{ad}$,

$$\text{find } \hat{\Omega}_o = \arg \min_{\Omega \in \mathcal{O}_{ad}} \mathcal{J}_o(Y(\Omega_o)) \tag{1}$$

of a cost functional $\mathcal{J}(Y(\Omega_o))$ depending on the solution $Y = Y(\Omega_o)$ of a state problem (e.g. under weak form)

$$Y \in \mathcal{Y}(\Omega_o): \quad \mathcal{A}_o(Y, W) = \mathcal{F}_o(W), \quad \forall\, W \in \mathcal{Y}(\Omega_o); \tag{2}$$

$\mathcal{A}_o(\cdot,\cdot)$ is a bilinear form and $\mathcal{F}_o(\cdot)$ is a linear form, both defined on the original domain Ω_o where the problem is defined; $\mathcal{Y}(\Omega_o)$ denotes a suitable functional space defined over Ω_o. Assuming that the shape Ω_o depends on a set of *input* parameters $\boldsymbol{\mu} = (\mu_1, \ldots, \mu_p) \in \mathcal{D} \subset \mathbb{R}^p$, problem (1)-(2) can be reduced to the following *parametric optimization* problem:

$$\text{find } \hat{\boldsymbol{\mu}} = \arg \min_{\boldsymbol{\mu} \in \mathcal{D}_{ad}} \mathcal{J}_o(Y(\boldsymbol{\mu})) \tag{3}$$

where $\mathcal{D}_{ad} \subseteq \mathcal{D}$ and $Y(\boldsymbol{\mu})$ solves

$$Y(\boldsymbol{\mu}) \in \mathcal{Y}(\Omega_o(\boldsymbol{\mu})): \quad \mathcal{A}_o(Y(\boldsymbol{\mu}), W; \boldsymbol{\mu}) = \mathcal{F}_o(W; \boldsymbol{\mu}), \quad \forall\, W \in \mathcal{Y}(\Omega_o(\boldsymbol{\mu})). \tag{4}$$

Our proposed approach to solve shape optimization problems is as follows. First we express the shape as a function of some *parametric input* $\boldsymbol{\mu}$, by means of a suitable parametrization of the geometry; in this way, an equivalent parametrized formulation of the flow problem – now embedding the shape as a parametric quantity – can be derived. At this point, we take advantage of the reduced basis (RB) method for parametrized PDEs [37], which provides the possibility to evaluate the *output* $\mathcal{J}_o(\cdot)$ very rapidly. At the outer level, an iterative procedure for the optimization is performed, now involving a very reduced version of the original problem. The RB method is premised upon a classical finite element (FE) method "truth" approximation space $\mathcal{Y}^{\mathcal{N}}$ of (typically very large) dimension $\mathcal{N}$ and is based on the use of "snapshot" FE solutions of the PDEs, corresponding to certain parameter values, as global approximation basis functions previously computed and stored. The RB framework thus requires a reference (parameter independent) domain Ω in order to compare, and combine, FE solutions that would be otherwise computed on different domains and grids. Moreover, this procedure enables to avoid shape deformation and remeshing that normally occur

Prepared using fldauth.cls
DOI: 10.1002/fld

at each step of an iterative optimization procedure. The reference domain Ω is related to the original domain $\Omega_o(\boldsymbol{\mu})$ through a parametric mapping $T(\cdot;\boldsymbol{\mu})$, such that $\Omega_o(\boldsymbol{\mu}) = T(\Omega;\boldsymbol{\mu})$. By tracing the problem (3)-(4) back on the reference domain Ω, we obtain the following parametrized formulation:

$$\begin{aligned} &\text{find } \hat{\boldsymbol{\mu}} = \arg \min_{\boldsymbol{\mu}\in\mathcal{D}_{ad}} s(\boldsymbol{\mu}) = \mathcal{J}(Y(\boldsymbol{\mu})) \quad \text{s.t.} \\ &Y(\boldsymbol{\mu}) \in \mathcal{Y}: \ \mathcal{A}(Y(\boldsymbol{\mu}), W; \boldsymbol{\mu}) = \mathcal{F}(W;\boldsymbol{\mu}), \ \forall W \in \mathcal{Y}. \end{aligned} \tag{5}$$

Following the so-called *discretize than optimize* approach [16], the standard Galerkin FE approximation of (5) is as follows:

$$\begin{aligned} &\text{find } \hat{\boldsymbol{\mu}} = \arg \min_{\boldsymbol{\mu}\in\mathcal{D}_{ad}} s^{\mathcal{N}}(\boldsymbol{\mu}) = \mathcal{J}(Y^{\mathcal{N}}(\boldsymbol{\mu})) \ \text{ s.t.} \\ &Y^{\mathcal{N}}(\boldsymbol{\mu}) \in \mathcal{Y}^{\mathcal{N}}: \ \mathcal{A}(Y^{\mathcal{N}}(\boldsymbol{\mu}), W; \boldsymbol{\mu}) = \mathcal{F}(W;\boldsymbol{\mu}), \ \forall W \in \mathcal{Y}^{\mathcal{N}}. \end{aligned} \tag{6}$$

The reduced basis method provides an efficient way to compute an approximation $Y_N(\boldsymbol{\mu})$ of $Y^{\mathcal{N}}(\boldsymbol{\mu})$ (and related output) by using a Galerkin projection on a reduced subspace made up of well-chosen FE solutions, corresponding to a specific choice $S_N = \{\boldsymbol{\mu}^1, \ldots, \boldsymbol{\mu}^N\}$ of parameter values. Indicating the RB space by

$$\mathcal{Y}_N^{\mathcal{N}} = \text{span}\{Y^{\mathcal{N}}(\boldsymbol{\mu}^n), n = 1, \ldots, N\}, \tag{7}$$

the RB formulation of (5) is as follows:

$$\begin{aligned} &\text{find } \hat{\boldsymbol{\mu}} = \arg \min_{\boldsymbol{\mu}\in\mathcal{D}_{ad}} s_N(\boldsymbol{\mu}) = \mathcal{J}(Y_N(\boldsymbol{\mu})) \ \text{ s.t.} \\ &Y_N(\boldsymbol{\mu}) \in \mathcal{Y}_N^{\mathcal{N}}: \ \mathcal{A}(Y_N(\boldsymbol{\mu}), W; \boldsymbol{\mu}) = \mathcal{F}(W;\boldsymbol{\mu}), \ \forall W \in \mathcal{Y}_N^{\mathcal{N}}. \end{aligned} \tag{8}$$

Thanks to the (considerably) reduced dimension $O(N) \ll O(\mathcal{N})$ of the linear systems obtained from RB approximation, we can provide both reliable results and rapid response in the real-time (e.g. parameter estimation) and multi-query contexts (e.g. optimal design/control).

2.2. *Reduced shape representations*

As anticipated in [23], a crucial point in shape optimization is the definition of the set of admissible shapes under which optimization can be performed. Following an increasing level of reduction, three different approaches can be envisaged:

- *Topological Shape Optimization*: in the most general case, we deal with the optimization of a shape by acting, during the optimization process, both on the position of its free boundary and on its topology [2, 9], as for example the inclusion of holes.
- *Geometrical Shape Optimization*: very often, the problem is formulated as the minimization of a cost functional (depending on both the shape and the solution of a PDE system) on a set of shapes with fixed topological properties; the position of the domain boundary under control is changed during the optimization process [43].
- *Parametric Shape Optimization*: this third approach is based on the possibility to describe the shape by means of some input parameters [2] and it is naturally the best framework where

Prepared using fldauth.cls
DOI: 10.1002/fld

reduced basis methods for P^{2}DEs can be exploited. Depending on the role played by input parameters, we can obtain three different subcases, depicted in Fig. 1:

1. input parameters represent *geometrical properties* (e.g. lenghts, angles, diameters, etc.) that identify different configurations in a family of shapes chosen *a priori*. In this way we obtain a simple but often restrictive description of domain shapes. For example, in previous works [34, 37, 40] bypass configurations have been modeled as "T-shaped" domains with a curved incoming branch;
2. input parameters are *variables describing shape boundary*, by means of explicit boundary parametrization or else involving given shapes families (such as Bézier curves, B-splines [5], etc.). The family of admissible shapes is wider, however deformations still depend on reference configuration and computational mesh;
3. input parameters are *free-form parameters*, such as perturbations applied to a lattice of mesh-independent control points [3,7,42]. In this case design parameters are not directly connected to geometrical properties, neither to the shape boundary we want to optimize.

In general, parametric shape optimization framework yields complexity reduction w.r.t. geometrical shape optimization (see the review [39] for a comparison of different options). In particular, free-form deformation techniques realize a very good trade-off between shape flexibility and using a low number of parameters, allowing therefore to achieve global computational efficiency by using a low dimensional optimization space [24]. A detailed description of this method will be provided in Sec. 4.

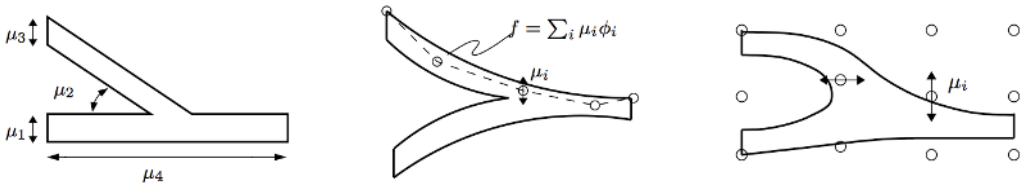

Figure 1. Different parametrization approaches: input parameters as geometrical properties (left), as variables describing shape boundary through a shapes family (middle), as free-form parameters (right).

By suitable parametrizations, shape optimization problems can thus be recast as optimal control problems dealing with geometrical (or design) parameters as control variables. The problem we consider in this work is related both to optimal design and flow control [16, 17, 27]; in the next section we present some aspects dealing with bypass surgery useful for drawing the mathematical formulation of the problem.

3. MATHEMATICAL MODELLING OF THE BYPASS PROBLEM

In this work we want to improve the results obtained in [33] by developing new tools of model order reduction (not considered in [1, 33]), and formulating the problem as a suitable parametrized shape optimization problem (as will be explained in Sect. 4). We aim at demonstrating the potential role of shape optimization techniques in designing bypass grafts, coupled with *(i)* suitable low-dimensional shape parametrization techniques for the configuration description and *(ii)* reduced basis methods

DOI: 10.1002/fld

for the solution of parametric PDE problems. The reader interested in medical and bio-engineering aspects related to the aorto-coronaric bypass problem can refer to Appendix A.

In the perspective of using low order methods for shape optimization featuring reasonable computational time, we adopt the steady Stokes equations (rather than the more appropriate Navier-Stokes equations, which are going to be used as "high fidelity" validation in feedback) for modelling low Reynolds blood flow in mid size arteries [13,33], like e.g. the coronary arteries. Besides, because of flow pulsatility we should consider unsteady equations during shape optimization with quantities averaged in time; however such a model would be too expensive from a computational point of view and its practical implementation in a shape optimization context.

3.1. Geometry description, state equations and system observation

To model the incoming branch of a bypass we consider a longitudinal section in the mean plane and the corresponding two-dimensional domain $\Omega_o(\boldsymbol{\mu})$; the steady Stokes equations [32] in $\Omega_o(\boldsymbol{\mu})$ read:

$$\begin{cases} -\nu\Delta\mathbf{v}(\boldsymbol{\mu}) + \nabla p(\boldsymbol{\mu}) = \mathbf{f} & \text{in } \Omega_o(\boldsymbol{\mu}) \\ \nabla\cdot\mathbf{v}(\boldsymbol{\mu}) = 0 & \text{in } \Omega_o(\boldsymbol{\mu}) \\ \mathbf{v}(\boldsymbol{\mu}) = \mathbf{0} & \text{on } \Gamma_w^o \\ \mathbf{v}(\boldsymbol{\mu}) = \mathbf{g}^D & \text{on } \Gamma_{in}^o \\ -p(\boldsymbol{\mu})\mathbf{n} + \nu\dfrac{\partial\mathbf{v}(\boldsymbol{\mu})}{\partial\mathbf{n}} = \mathbf{g}^N & \text{on } \Gamma_{out}^o, \end{cases} \tag{9}$$

where $(\mathbf{v}(\boldsymbol{\mu}), p(\boldsymbol{\mu}))$ are the velocity and the pressure fields, for some given $\mathbf{f}$, $\mathbf{g}^D$, $\mathbf{g}^N$; $\mathbf{n}$ is the normal unit vector on the boundary $\partial\Omega_o(\boldsymbol{\mu})$, which is partitioned as in Fig. 2: Γ_{in}^o is the inflow boundary, Γ_{out}^o the outflow boundary and Γ_w^o the boundary corresponding to the arterial wall. We assume that on inflow and outflow sections the normal unit vector will not change after geometrical transformation/parametrization.

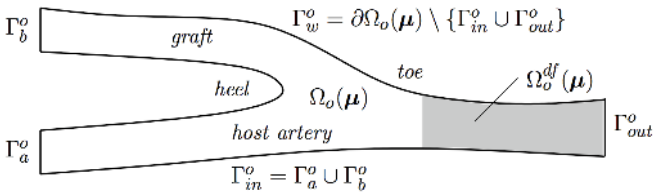

Figure 2. Idealized two-dimensional bypass anastomosis and notation used for domain and boundary; $\Omega_o^{df}(\boldsymbol{\mu})$ is the down-field region where observation will be made.

We set $\Gamma_D^o = \Gamma_{in}^o \cup \Gamma_w^o$. The inflow boundary Γ_{in}^o is given by two different inflow sections: the bypass inflow section Γ_b^o and the stenosed artery section Γ_a^o. No-slip conditions are imposed on Γ_w, while homogeneous (free-stress) Neumann conditions are imposed on the outflow section Γ_{out}^o. Concerning inflow boundary conditions, we impose a Poiseuille parabolic profile on Γ_b^o. Indeed, the Womersley number [13, 44] for blood flow in coronary arteries is $Wo \approx 2.1$ and a steady Womersley profile can be assimilated at a simpler Poiseuille flow. Then we consider two different cases for the artery section Γ_a^o, according that we have either complete occlusion ($\mathbf{g}^D = 0$ on Γ_a^o) or a partial occlusion (residual flow $\mathbf{g}^D \neq 0$ on Γ_a^o). Inflow peak velocity is $\tilde{v} = 30cm\,s^{-1}$, while arterial diameter is about $0.3cm$; blood dynamic viscosity is $\mu = 0.04g\,cm^{-1}\,s^{-1}$, blood density

DOI: 10.1002/fld

$\rho = 1 g\, cm^{-3}$, thus yielding a kynematic viscosity $\nu = \mu/\rho = 0.04 cm^2\, s^{-1}$ and a Reynolds number $Re = \tilde{v}D/\nu$ of order 10^2.

Let us now characterize the abstract framework (3)-(4). Let us denote $Y(\boldsymbol{\mu}) = (\mathbf{v}(\boldsymbol{\mu}), p(\boldsymbol{\mu}))$, $W = (\mathbf{w}, q)$ and

$$\mathcal{A}_o(Y(\boldsymbol{\mu}), W; \boldsymbol{\mu}) = a_o(\mathbf{u}(\boldsymbol{\mu}), \mathbf{w}; \boldsymbol{\mu}) + b_o(p(\boldsymbol{\mu}), \mathbf{w}; \boldsymbol{\mu}) + b_o(q, \mathbf{u}(\boldsymbol{\mu}); \boldsymbol{\mu}), \tag{10}$$

where

$$a_o(\mathbf{u}, \mathbf{w}; \boldsymbol{\mu}) = \int_{\Omega_o(\boldsymbol{\mu})} \frac{\partial \mathbf{u}}{\partial x_{oi}} \nu_{ij}^o \frac{\partial \mathbf{w}}{\partial x_{oj}} d\Omega_o, \qquad \nu_{ij}^o = \nu \delta_{ij},$$

$$b_o(p, \mathbf{w}; \boldsymbol{\mu}) = -\int_{\Omega_o(\boldsymbol{\mu})} p \chi_{ij}^o \frac{\partial w_j}{\partial x_{oi}} d\Omega_o, \qquad \chi_{ij}^o = \delta_{ij},$$

being δ_{ij} the Kronecker symbol and $1 \le i, j \le 2$, represents the single components of coordinates and vectorial quantities. In the same way,

$$\mathcal{F}_o(W; \boldsymbol{\mu}) = \langle F_o^s, \mathbf{w} \rangle + \langle F_o^l, \mathbf{w} \rangle + \langle G_o^l, q \rangle \tag{11}$$

where

$$\langle F_o^s, \mathbf{w} \rangle = \int_{\Omega_o(\boldsymbol{\mu})} \mathbf{f} \cdot \mathbf{w} d\Omega_o + \int_{\Gamma_{out}^o} \mathbf{g}^N \cdot \mathbf{w} d\Gamma_o$$

is a source term and

$$\langle F_o^l, \mathbf{w} \rangle = -a_o(R_o, \mathbf{w}; \boldsymbol{\mu}), \quad \langle G_o^l, q \rangle = -b_o(q, R_o; \boldsymbol{\mu})$$

are the terms related to the lifting of nonhomogeneous Dirichlet boundary conditions. Here $\mathcal{Y}(\Omega_o(\boldsymbol{\mu})) = \mathcal{X}(\boldsymbol{\mu}) \times \mathcal{Q}(\boldsymbol{\mu})$, being $\mathcal{X}(\boldsymbol{\mu}) = (H^1_{0,\Gamma_D}(\Omega_o(\boldsymbol{\mu})))^2$ the velocity space, $\mathcal{Q}(\boldsymbol{\mu}) = L^2(\Omega_o(\boldsymbol{\mu}))$ the pressure space, and $H^1_{0,\Gamma_D}(\Omega) = \{v \in H^1(\Omega) : v|_{\Gamma_D} = 0\}$, respectively; $R_o \in (H^1(\Omega_o(\boldsymbol{\mu})))^2$ is a lifting function such that $R_o|_{\Gamma_{in}^o} = \mathbf{g}^D$. We denote $\tilde{\mathbf{v}} = \mathbf{v} - R_o$, so that $\tilde{\mathbf{v}}|_{\Gamma_D^o} = \mathbf{0}$ and $\nabla \tilde{\mathbf{v}} = \nabla \mathbf{v} - \nabla R_o$. For the sake of simplicity, we still denote $\tilde{\mathbf{v}}$ with $\mathbf{v}$ in the sequel, as no ambiguity occurs.

With the goal of reducing the blood vorticity $\nabla \times \mathbf{v}(\boldsymbol{\mu})$ in the down-field zone $\Omega_o^{df}(\boldsymbol{\mu}) \subseteq \Omega_o(\boldsymbol{\mu})$ of the incoming branch of the bypass, we introduce a suitable parametric output; we thus control the system by minimizing the following quantity:

$$s_o(\boldsymbol{\mu}) = \mathcal{J}_o(\mathbf{v}(\boldsymbol{\mu})) = \frac{1}{2} \int_{\Omega_o(\boldsymbol{\mu})} Q(\mathbf{v}(\boldsymbol{\mu})) d\Omega_o, \tag{12}$$

being

$$Q(\mathbf{w}) = |\nabla \times \mathbf{w}|^2 \mathbb{I}_{\Omega_o^{df}(\boldsymbol{\mu})},$$

and $\mathbb{I}_D(\cdot)$ the indicator function of the domain D. With this choice of the cost functional and the flow model, existence of solutions of problem (1)-(2) is in general stated [17, 19] for

$$\mathcal{O}_{ad} = \{\Omega_o \in \mathcal{U}_L : |\Omega_o| \le |D|,\ \overline{\Omega}_o \cap D = \Gamma_{in}^o\},$$

DOI: 10.1002/fld

where $\mathcal{U}_L = \{\Omega_o \subset D, \Omega_o \text{ open Lipschitz domain}\}$ and D is a given fixed rectangle of area $|D|$; first order necessary conditions can be derived by either introducing a suitable adjoint problem [6,33,34] or using the approach based on Lagrange multipliers [16].

3.2. Parametrized formulation

By tracing the forms (10)-(11) back on the reference domain Ω, the parametrized formulation of the Stokes problem reads: find $Y(\boldsymbol{\mu}) = (\mathbf{v}(\boldsymbol{\mu}), p(\boldsymbol{\mu})) \in \mathcal{Y}$ such that

$$\mathcal{A}(Y(\boldsymbol{\mu}), W; \boldsymbol{\mu}) = \mathcal{F}(W; \boldsymbol{\mu}), \quad \forall W \in \mathcal{Y}, \tag{13}$$

where

$$\mathcal{A}(Y(\boldsymbol{\mu}), W; \boldsymbol{\mu}) = a(\mathbf{v}(\boldsymbol{\mu}), \mathbf{w}; \boldsymbol{\mu}) + b(p(\boldsymbol{\mu}), \mathbf{w}; \boldsymbol{\mu}) + b(q, \mathbf{v}(\boldsymbol{\mu}); \boldsymbol{\mu}),$$

$$a(\mathbf{v}, \mathbf{w}; \boldsymbol{\mu}) = \int_\Omega \frac{\partial \mathbf{v}}{\partial x_i} \nu_{ij}(\boldsymbol{\mu}) \frac{\partial \mathbf{w}}{\partial x_j} d\Omega, \qquad b(p, \mathbf{w}; \boldsymbol{\mu}) = -\int_\Omega p \chi_{ij}(\boldsymbol{\mu}) \frac{\partial w_j}{\partial x_i} d\Omega;$$

and

$$\mathcal{F}(W; \boldsymbol{\mu}) = \langle F^s, \mathbf{w} \rangle + \langle F^l, \mathbf{w} \rangle + \langle G^l, q \rangle,$$

$$\langle F^s, \mathbf{w} \rangle = \int_\Omega \mathbf{f} \cdot \mathbf{w} |\boldsymbol{J}_T| d\Omega + \int_{\Gamma_{out}} \mathbf{g}^N \cdot \mathbf{w} |\boldsymbol{J}_T \mathbf{t}| d\Gamma,$$

$$\langle F^l, \mathbf{w} \rangle = -a(R, \mathbf{w}; \boldsymbol{\mu}), \quad \langle G^l, q \rangle = -b(q, R; \boldsymbol{\mu}).$$

Notations are as follows:

- $\mathcal{Y} = \mathcal{X} \times \mathcal{Q}$, being $\mathcal{X} = (H^1_{0,\Gamma_D}(\Omega))^2$ and $\mathcal{Q} = L^2(\Omega)$, respectively;
- $R \in (H^1(\Omega))^2$ is such that $R|_{\Gamma_D} = \mathbf{g}^D$ and $\mathbf{t}$ denotes the unit tangential vector to $\partial\Omega$;
- the transformation tensor in the bilinear form $a(\cdot, \cdot; \boldsymbol{\mu})$ is defined as

$$\boldsymbol{\nu}(\mathbf{x}, \boldsymbol{\mu}) = \boldsymbol{J}_T^{-1} \boldsymbol{\nu}^o \boldsymbol{J}_T^{-T} |\boldsymbol{J}_T|; \tag{14}$$

- the tensor used in the bilinear form $b(\cdot, \cdot; \boldsymbol{\mu})$ is given by

$$\boldsymbol{\chi}(\mathbf{x}, \boldsymbol{\mu}) = \boldsymbol{J}_T^{-1} |\boldsymbol{J}_T|, \tag{15}$$

  where $\boldsymbol{J}_T = \boldsymbol{J}_T(\mathbf{x}, \boldsymbol{\mu})$ denotes the Jacobian of $T(\mathbf{x}, \boldsymbol{\mu})$ and $|\boldsymbol{J}_T|$ its determinant.

A necessary condition for the well-posedness of (13) is the Babuška "inf-sup" condition [28], which can be stated as follows. Let us define the norm on the product space $\mathcal{Y}$ as

$$\|Y\|^2_{\mathcal{Y}} := \|\mathbf{v}\|^2_{\mathcal{X}} + \|p\|^2_{\mathcal{Q}}, \qquad \forall Y = (\mathbf{v}, p) \in \mathcal{Y} = \mathcal{X} \times \mathcal{Q};$$

moreover, let us introduce the *supremizer operator* [28] $T^{\boldsymbol{\mu}} : \mathcal{Y} \to \mathcal{Y}$ such that, for any $W \in \mathcal{Y}$,

$$(T^{\boldsymbol{\mu}} W, V)_{\mathcal{Y}} = \mathcal{A}(W, V; \boldsymbol{\mu}), \qquad \forall\, Y \in \mathcal{Y} \tag{16}$$

DOI: 10.1002/fld

and indicate with $\beta(\boldsymbol{\mu})$ the following quantity,

$$\beta(\boldsymbol{\mu}) := \inf_{W \in \mathcal{Y}} \sup_{V \in \mathcal{Y}} \frac{\mathcal{A}(W, V; \boldsymbol{\mu})}{\|W\|_{\mathcal{Y}} \|V\|_{\mathcal{Y}}}, \tag{17}$$

so that

$$\beta(\boldsymbol{\mu}) \|W\|_{\mathcal{Y}} \|T^{\boldsymbol{\mu}} W\|_{\mathcal{Y}} \leq \mathcal{A}(W, T^{\boldsymbol{\mu}} W; \boldsymbol{\mu}), \qquad \forall\, W \in \mathcal{Y}. \tag{18}$$

We require the following Babuška "inf-sup" stability condition:

$$\exists\, \beta_0 > 0 : \quad \beta(\boldsymbol{\mu}) \geq \beta_0 > 0, \qquad \forall\, \boldsymbol{\mu} \in \mathcal{D}; \tag{19}$$

β_0 is said "inf-sup" stability constant. Moreover, we require that the bilinear form $\mathcal{A}(\cdot; \cdot; \boldsymbol{\mu})$ is continuous, i.e. the continuity constant

$$\gamma(\boldsymbol{\mu}) := \sup_{V \in \mathcal{Y}} \sup_{W \in \mathcal{Y}} \frac{\mathcal{A}(V, W; \boldsymbol{\mu})}{\|W\|_{\mathcal{Y}} \|V\|_{\mathcal{Y}}}$$

is finite for all $\boldsymbol{\mu} \in \mathcal{D}$, as well as that the linear form $\mathcal{F}(\cdot; \boldsymbol{\mu})$ is continuous for all $\boldsymbol{\mu} \in \mathcal{D}$. All these hypotheses are verified whether $\nu_{ij}(\cdot; \boldsymbol{\mu}) \in L^\infty(\Omega)$, $\chi_{ij}(\cdot; \boldsymbol{\mu}) \in L^\infty(\Omega)$ for all $\boldsymbol{\mu} \in \mathcal{D}$ and $\mathbf{f} \in (L^2(\Omega))^2$, $\mathbf{g}^D \in (L^2(\Gamma_D))^2$, $\mathbf{g}^N \in (L^2(\Gamma_N))^2$.

Concerning the parametrized expression of the output to be minimized appearing in (5), by tracing (12) back to the reference domain Ω we have

$$s(\boldsymbol{\mu}) = \mathcal{J}(\mathbf{v}(\boldsymbol{\mu})) = \frac{1}{2} \int_\Omega Q \circ T(\mathbf{v}(\boldsymbol{\mu})) |\boldsymbol{J}_T|\, d\Omega. \tag{20}$$

Well posedness and optimality conditions for (5) can be easily derived using standard arguments and techniques [2]. Hence, the original problem has been reformulated on a reference configuration, resulting in a parametrized problem where the effect of geometry variations is traced back onto its parametrized transformation tensors.

4. SHAPE PARAMETRIZATION BY FREE-FORM DEFORMATION TECHNIQUES

Since shape representation is highly specific problem-dependent, various methods have been proposed; a classical approach in *geometrical shape optimization* is the so-called *local boundary variation* technique [2, 27], while the most common shape representation adopted in *parametric shape optimization* problems is the explicit *boundary shape parametrization* [5, 8, 10]. The former uses the discrete nodes of the triangulation lying on the boundary as design variables and their displacement for the shape deformation. Since very fine meshes are needed for complex shapes or flows, the number of design variables may become very large, leading to very high computational costs. The latter involves shapes families (mainly polynomial or *spline* functions) depending on a small set of control points, even if a larger number of parameters may be required to represent complex shapes. Nevertheless, after each shape deformation, remeshing is in order.

DOI: 10.1002/fld

An alternative approach, potentially able to be quite versatile with more complex shapes in order to avoid remeshing, is the free-form deformation (FFD) technique, in which it is the deformation of an initial design (and not the geometry itself) to be parametrized. The technique consists of embedding the shape to be deformed inside a control area and then of modifying – by acting on a lattice of control points – the metrics of this space and thus the shape embedded into it, rather than modifying the shape directly. A modification of the control points position thus results in a deformation inside the control area and, automatically, of the computational FE mesh. Based on tensor product of splines, FFD inherits from boundary parametrization techniques the possibility to handle with global deformations by acting on a small set of control points [3, 7], but provides an easier tool since any explicit parametrization is required [24]. FFD coupled with reduced basis methods has previously been proposed as a parametrization technique for inverse airfoils design [23] and thermal flows control [38]; extensions of this methodology to three-dimensional geometries are possible, even if complex from the implementation point of view. In this work we aim at enhancing the computational performance in the shape optimization process by reduced order modelling for viscous flows, and further developing what started in [23] for potential flows.

Given a fixed rectangular domain D containing the reference domain $\Omega \subset D$, we introduce an affine map $\hat{\mathbf{x}} = \Psi(\mathbf{x})$, $\mathbf{x} \in D$, such that $\Psi(D) = (0,1)^2 \equiv \hat{D}$ with $\Psi(\cdot)$ a monotonic function, in order to define FFD in a simpler way in the coordinates $\hat{\mathbf{x}} = (\hat{x}_1, \hat{x}_2)$ of the spline parameter space $(0,1)^2$. On $\hat{D}$ we thus select an ordered mesh of $(L+1) \times (M+1)$ unperturbed control points

$$\mathbf{P}_{l,m} = [l/L, m/M]^T, \qquad l = 0, \dots, L, \quad m = 0, \dots, M$$

and modify the object by moving control points to a new position. The corresponding perturbed control points $\mathbf{P}^o_{l,m}$ are specified by a set of $(L+1)(M+1)$ parameter vectors $\boldsymbol{\mu}_{l,m} \in \mathbb{R}^2$

$$\mathbf{P}^o_{l,m}(\boldsymbol{\mu}_{l,m}) = \mathbf{P}_{l,m} + \boldsymbol{\mu}_{l,m}, \tag{21}$$

giving in all $2(L+1)(M+1)$ possible degrees of freedom. As often as not, only small subsets of these are selected as design variables if we want to perform a sensible geometrical model order reduction; moreover, several rows or columns of control points can be fixed to obtain desired levels of continuity or to "anchor" certain parts of the domain. In general, among the control points $\mathbf{P}_{l,m}$, we indicate the effectively free scalar-valued parameters chosen as design variables as $\mu_1, \dots, \mu_p$ – each corresponding to the displacement of a control point in either the $\hat{x}_1$ or the $\hat{x}_2$ direction, i.e. to one of the components of a vector $\boldsymbol{\mu}_{l,m}$ – and define the parametric map $\hat{T}(\cdot;\boldsymbol{\mu}) : \hat{D} \to \hat{D}_o(\boldsymbol{\mu})$ by which the uploaded geometry is computed as follows:

$$\hat{T}(\hat{\mathbf{x}};\boldsymbol{\mu}) = \left(\sum_{l=0}^{L} \sum_{m=0}^{M} b^{L,M}_{l,m}(\hat{\mathbf{x}}) \mathbf{P}^o_{l,m}(\boldsymbol{\mu}_{l,m}) \right), \tag{22}$$

where

$$b^{L,M}_{l,m}(\hat{\mathbf{x}}) = b^L_l(\hat{x}_1) b^M_m(\hat{x}_2) = \binom{L}{l} \binom{M}{m} (1-\hat{x}_1)^{L-l} \hat{x}_1^l (1-\hat{x}_2)^{M-m} \hat{x}_2^m$$

DOI: 10.1002/fld

are tensor products of the unidimensional *Bernstein basis polynomials* defined on $\hat{D}$ by

$$b_l^L(\hat{x}_1) = \binom{L}{l} \hat{x}_1^l (1-\hat{x}_1)^{L-l}, \qquad b_m^M(\hat{x}_2) = \binom{M}{m} \hat{x}_2^m (1-\hat{x}_2)^{M-m}.$$

Finally, the FFD mapping $T(\cdot, \boldsymbol{\mu})$ is obtained as the composition

$$T(\cdot; \boldsymbol{\mu}) : D \to D_o(\boldsymbol{\mu}), \qquad T(\mathbf{x}; \boldsymbol{\mu}) = \Psi^{-1} \circ \hat{T} \circ \Psi(\mathbf{x}; \boldsymbol{\mu}); \tag{23}$$

in particular, the parametrized domain $\Omega_o(\boldsymbol{\mu})$ is obtained as $\Omega_o(\boldsymbol{\mu}) = \Psi^{-1} \circ \hat{T} \circ \Psi(\Omega; \boldsymbol{\mu})$; see Fig. 3 for a representation of the mapping construction.

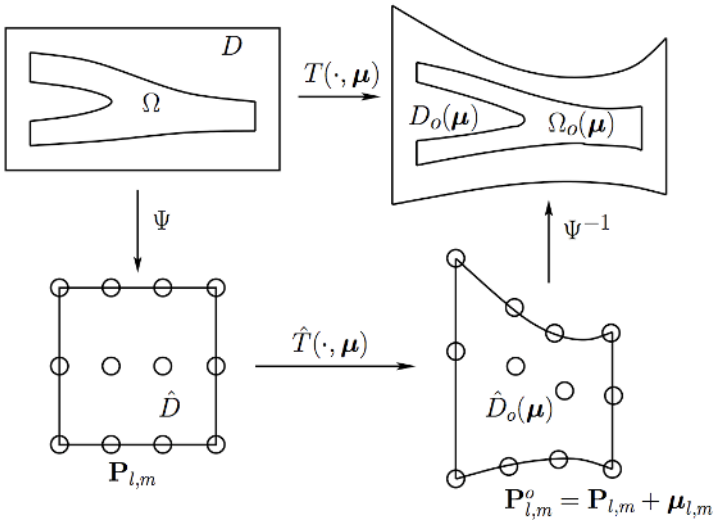

Figure 3. Schematic diagram of the FFD technique: unperturbed control points $\mathbf{P}_{l,m}$, perturbed control points $\mathbf{P}^o_{l,m}(\boldsymbol{\mu}_{l,m})$, map $\hat{\mathbf{x}} = \Psi(\mathbf{x})$, $\hat{T}(\hat{\mathbf{x}}; \boldsymbol{\mu})$ and resulting FFD map $T(\mathbf{x}; \boldsymbol{\mu}) = (\Psi^{-1} \circ \hat{T} \circ \Psi)(\mathbf{x}; \boldsymbol{\mu})$.

Since only the degrees of freedom corresponding to $\mu_1, \ldots, \mu_p$ will play the role of design variables, the map (22) can be seen as a function of $\boldsymbol{\mu} = (\mu_1 \ldots, \mu_p)$; nevertheless, also other control points – which do not correspond to effective design variables – obviously go under displacement. The number and position of control points chosen have a deep impact on FFD flexibility: it is crucial to maximize the influence of the control points by placing them close to the more sensitive regions of the configuration.

Using the inverse of $T(\cdot; \boldsymbol{\mu})$ we can get the parametrized formulation of the problem (13) by mapping the equations back onto the reference domain Ω and computing the transformation tensors (14) and (15). Compared to classical strategies such as boundary shape parametrization, FFD techniques lead to low-dimensional parametrizations without loss of accuracy, since perturbations on parameters yield smooth shape deformations even if control points are not related to the shape boundary. We next introduce reduced basis methods for approximating in a rapid and reliable way solutions to (13) and then evaluating the parametric output (20).

DOI: 10.1002/fld

5. REDUCED BASIS METHODS FOR NONCOERCIVE PDES

Our approach to shape optimization takes advantage of *reduced basis* (RB) method for rapid and reliable prediction of outputs associated with parametrized PDEs. In particular, reliability is ensured by rigorous a posteriori estimations for the error in the RB approximation w.r.t. truth FE discretization [29, 31, 37]; rapid response is ensured by an Offline–Online computational strategy which minimizes marginal cost and a rapidly convergent RB space assembling, based on a *greedy algorithm* [37]. In this section we review all these aspects, in the general framework of noncoercive problems.

Let us now characterize the FE formulation (6) to the Stokes case under analysis, where $\mathcal{Y}^{\mathcal{N}} = \mathcal{X}^{\mathcal{N}} \times \mathcal{Q}^{\mathcal{N}}$, $Y^{\mathcal{N}}(\boldsymbol{\mu}) = (\mathbf{v}^{\mathcal{N}}(\boldsymbol{\mu}), p^{\mathcal{N}}(\boldsymbol{\mu}))$, being $\mathbf{v}^{\mathcal{N}}(\boldsymbol{\mu}) \in \mathcal{X}^{\mathcal{N}}$ and $p^{\mathcal{N}}(\boldsymbol{\mu}) \in \mathcal{Q}^{\mathcal{N}}$ the FE approximations of the velocity and the pressure, respectively. The dimension $\mathcal{N} = \mathcal{N}_{\mathcal{X}} + \mathcal{N}_{\mathcal{Q}}$ of the FE spaces is thus taken large enough in order to neglect the differences $\|\mathbf{v}^{\mathcal{N}}(\boldsymbol{\mu}) - \mathbf{v}(\boldsymbol{\mu})\|_{\mathcal{X}(\Omega)}$ and $\|p^{\mathcal{N}}(\boldsymbol{\mu}) - p(\boldsymbol{\mu})\|_{\mathcal{Q}(\Omega)}$, so that it can be effectively considered as a"truth" approximation. In our case $\mathcal{X}^{\mathcal{N}} \times \mathcal{Q}^{\mathcal{N}}$ is the space of Taylor-Hood $\mathbb{P}_2 - \mathbb{P}_1$ elements; however, this choice is not restrictive, the whole construction keeps holding for other spaces combinations as well.

5.1. *Reduced basis approximation: formulation and main features*

The RB method computes an approximation of $(\mathbf{v}^{\mathcal{N}}(\boldsymbol{\mu}), p^{\mathcal{N}}(\boldsymbol{\mu}))$ by using global approximation spaces made up of well-chosen FE solutions, i.e. corresponding to specific choices of the parameter values. The basic assumption is that the solution to (13) depends smoothly on the parameters, whence the parametric manifold of solutions in $\mathcal{X} \times \mathcal{Q}$ is smooth too and can be approximated by selecting, among classical FE solutions, some "snapshot" solutions. Let us take a relatively small set of parameter values $S_N = \{\boldsymbol{\mu}^1, \ldots, \boldsymbol{\mu}^N\}$ and consider the corresponding FE solutions $(\mathbf{v}^{\mathcal{N}}(\boldsymbol{\mu}^1), p^{\mathcal{N}}(\boldsymbol{\mu}^1)), \ldots, (\mathbf{v}^{\mathcal{N}}(\boldsymbol{\mu}^N), p^{\mathcal{N}}(\boldsymbol{\mu}^N))$, where typically $N \ll \mathcal{N}$. We define the *reduced basis pressure space* $\mathcal{Q}_N^{\mathcal{N}} \subset \mathcal{Q}^{\mathcal{N}}$ as

$$\mathcal{Q}_N^{\mathcal{N}} = \text{span}\{\zeta_n := p^{\mathcal{N}}(\boldsymbol{\mu}^n),\ n = 1, \ldots, N\}.$$

The *reduced basis velocity space* $\mathcal{X}_N^{\mathcal{N}} \subset \mathcal{X}^{\mathcal{N}}$ can be built as

$$\mathcal{X}_N^{\mathcal{N}} = \text{span}\{\boldsymbol{\sigma}_n := \mathbf{v}^{\mathcal{N}}(\boldsymbol{\mu}^n),\ T_p^{\boldsymbol{\mu}}\zeta_n,\ n = 1, \ldots, N\},$$

where $T_p^{\boldsymbol{\mu}} : \mathcal{Q}_N^{\mathcal{N}} \to \mathcal{X}_N^{\mathcal{N}}$ is the so-called *inner supremizer operator* acting on pressure term,

$$(T_p^{\boldsymbol{\mu}} q, \mathbf{w})_{\mathcal{X}} = b(q, \mathbf{w}; \boldsymbol{\mu}) \quad \forall\, \mathbf{w} \in \mathcal{X}_N^{\mathcal{N}}. \tag{24}$$

With the above definitions of the RB spaces, the following LBB condition [34, 35] holds:

$$\inf_{q \in \mathcal{Q}_N^{\mathcal{N}}} \sup_{\mathbf{w} \in \mathcal{X}_N^{\mathcal{N}}} \frac{b(q, \mathbf{w}; \boldsymbol{\mu})}{\|\mathbf{w}\|_{\mathcal{X}} \|q\|_{\mathcal{Q}}} =: \beta_N(\boldsymbol{\mu}) \geq \beta(\boldsymbol{\mu}) \geq \beta_0 > 0, \qquad \forall\, \boldsymbol{\mu} \in \mathcal{D}, \tag{25}$$

where $\beta(\boldsymbol{\mu})$ and β_0 are the same constants as in (17) and (19). In order to develop both the a posteriori error estimation and the Offline-Online computational procedure, let us explicit the RB

Prepared using fldauth.cls
DOI: 10.1002/fld

approximation of the Stokes problem (13), obtained through a Galerkin projection onto $\mathcal{X}_N^{\mathcal{N}} \times \mathcal{Q}_N^{\mathcal{N}}$: find $Y_N(\boldsymbol{\mu}) = (\mathbf{v}_N(\boldsymbol{\mu}), p_N(\boldsymbol{\mu})) \in \mathcal{Y}_N = \mathcal{X}_N^{\mathcal{N}} \times \mathcal{Q}_N^{\mathcal{N}}$ such that

$$\begin{cases} a(\mathbf{v}_N(\boldsymbol{\mu}), \mathbf{w}; \boldsymbol{\mu}) + b(p_N(\boldsymbol{\mu}), \mathbf{w}; \boldsymbol{\mu}) = \langle F^s, \mathbf{w} \rangle + \langle F^l, \mathbf{w} \rangle & \forall\ \mathbf{w} \in \mathcal{X}_N^{\mathcal{N}} \\ b(q, \mathbf{v}_N(\boldsymbol{\mu}); \boldsymbol{\mu}) = \langle G, q \rangle & \forall\ q \in \mathcal{Q}_N^{\mathcal{N}}. \end{cases} \tag{26}$$

Condition (25) ensures well-posedness of (26). In practice, the Gram-Schmidt orthonormalization procedure [34] has to be adopted, to build basis for pressure and velocity RB spaces that guarantee algebraic stability (i.e. the condition number of the resulting RB system is relatively small); hence, the RB solution can be written as

$$\mathbf{v}_N(\boldsymbol{\mu}) = \sum_{j=1}^{2N} v_{Nj}(\boldsymbol{\mu}) \boldsymbol{\sigma}_j, \qquad p_N(\boldsymbol{\mu}) = \sum_{l=1}^{N} p_{Nl}(\boldsymbol{\mu}) \zeta_l, \tag{27}$$

where $\{\boldsymbol{\sigma}_j\}_{j=1}^{2N}$ and $\{\zeta_l\}_{l=1}^{N}$ are orthonormal basis for $\mathcal{X}_N^{\mathcal{N}}$ and $\mathcal{Q}_N^{\mathcal{N}}$, respectively. Since $N \ll \mathcal{N}$, problem (26) has a much lower dimension than the corresponding FE approximation in (6).

5.2. Reduced basis space assembling and error estimation

The choice of the snapshot solutions is crucial for the accuracy of the RB approximation and is operated using the following *greedy* algorithm [31, 37]. Let $\Xi_{train} \subset \mathcal{D}$ be a (sufficiently rich) finite training sample of parameter points chosen using a uniform distribution on $\mathcal{D}$; given the first parameter value $\boldsymbol{\mu}^1$ and a sharp, rigorous and inexpensive error bound $\Delta_N(\boldsymbol{\mu})$ for the norm such that, for the generic approximation $Y_n(\boldsymbol{\mu}) = (\mathbf{v}_n(\boldsymbol{\mu}), p_n(\boldsymbol{\mu})) \in \mathcal{Y}_n$, $n = 1, \ldots, N$,

$$\|Y^{\mathcal{N}}(\boldsymbol{\mu}) - Y_n(\boldsymbol{\mu})\|_{\mathcal{Y}} \leq \Delta_n(\boldsymbol{\mu}) \quad \text{for all } \boldsymbol{\mu} \in \Xi_{train},$$

we choose the remaining parameter values (and corresponding snapshot solutions) as

$$\boldsymbol{\mu}^n := \arg \max_{\boldsymbol{\mu} \in \Xi_{train}} \Delta_{n-1}(\boldsymbol{\mu}), \quad \text{for } n = 2, \ldots, N$$

until an error tolerance ε_{tol}^{RB} a priori fixed is achieved:

$$\Delta_N(\boldsymbol{\mu}) \leq \varepsilon_{tol}^{RB} \quad \text{for all } \boldsymbol{\mu} \in \Xi_{train}.$$

The error bound $\Delta_N(\boldsymbol{\mu})$ is also used for estimating the error of the RB approximation w.r.t. the "truth" FE solution [31, 37] and can be defined introducing the residuals

$$r_N^v(\mathbf{w}; \boldsymbol{\mu}) := \langle F^s, \mathbf{w} \rangle + \langle F^l, \mathbf{w} \rangle - a(\mathbf{v}_N(\boldsymbol{\mu}), \mathbf{w}; \boldsymbol{\mu}) - b(p_N(\boldsymbol{\mu}), \mathbf{w}; \boldsymbol{\mu}),$$
$$r_N^p(q; \boldsymbol{\mu}) := \langle G^l, q \rangle - b(q, \mathbf{v}_N(\boldsymbol{\mu}); \boldsymbol{\mu}).$$

Note that

$$r_N^v(\mathbf{w}; \boldsymbol{\mu}) = a(\mathbf{v}^{\mathcal{N}}(\boldsymbol{\mu}) - \mathbf{v}_N(\boldsymbol{\mu}), \mathbf{w}; \boldsymbol{\mu}) + b(p^{\mathcal{N}}(\boldsymbol{\mu}) - p_N(\boldsymbol{\mu}), \mathbf{w}; \boldsymbol{\mu}) \quad \forall\ \mathbf{w} \in \mathcal{X}^{\mathcal{N}},$$
$$r_N^p(q; \boldsymbol{\mu}) = b(q, \mathbf{v}^{\mathcal{N}}(\boldsymbol{\mu}) - \mathbf{v}_N(\boldsymbol{\mu}); \boldsymbol{\mu}) \quad \forall\ q \in \mathcal{Q}^{\mathcal{N}}$$

DOI: 10.1002/fld

or, equivalently, with $r_N(W;\boldsymbol{\mu}) := r_N^v(\mathbf{w};\boldsymbol{\mu}) + r_n^p(q;\boldsymbol{\mu})$,

$$r_N(W;\boldsymbol{\mu}) = \mathcal{A}(Y^{\mathcal{N}}(\boldsymbol{\mu}) - Y_N(\boldsymbol{\mu}), W;\boldsymbol{\mu}) \quad \forall\, W \in \mathcal{Y}^{\mathcal{N}}.$$

Using the condition (18), we have the following residual-based estimator

$$\Delta_N(\boldsymbol{\mu}) = \frac{\|r_N(\cdot;\boldsymbol{\mu})\|_{\mathcal{Y}'}}{\beta_{LB}(\boldsymbol{\mu})} \geq \|Y^{\mathcal{N}}(\boldsymbol{\mu}) - Y_N\|_{\mathcal{Y}} \tag{28}$$

where $\|\cdot\|_{\mathcal{Y}'}$ is the dual norm of the residual defined as

$$\|r_N(\cdot;\boldsymbol{\mu})\|_{\mathcal{Y}'} = \sup_{V\in\mathcal{Y}^{\mathcal{N}}} \frac{r_N(V;\boldsymbol{\mu})}{\|V\|_{\mathcal{Y}}}$$

and $\beta_{LB}(\boldsymbol{\mu})$ is a computable lower bound for the inf-sup constant $\beta(\boldsymbol{\mu})$ [22]. An alternative expression of the error estimator (28) is given by

$$\|\mathbf{v}^{\mathcal{N}}(\boldsymbol{\mu}) - \mathbf{v}_N(\boldsymbol{\mu})\|_{\mathcal{X}}^2 + \|p^{\mathcal{N}}(\boldsymbol{\mu}) - p_N(\boldsymbol{\mu})\|_{\mathcal{Q}}^2 \leq \frac{1}{\beta_{LB}^2(\boldsymbol{\mu})} \left(\|r_N^v(\cdot\,;\boldsymbol{\mu})\|_{\mathcal{X}'}^2 + \|r_N^p(\cdot\,;\boldsymbol{\mu})\|_{\mathcal{Q}'}^2\right)$$

where

$$\|r_N^v(\cdot\,;\boldsymbol{\mu})\|_{\mathcal{X}'} = \sup_{\mathbf{w}\in\mathcal{X}^{\mathcal{N}}} \frac{r_N^v(\mathbf{w};\boldsymbol{\mu})}{\|\mathbf{w}\|_{\mathcal{X}}}, \qquad \|r_N^p(\cdot\,;\boldsymbol{\mu})\|_{\mathcal{Q}'} = \sup_{q\in\mathcal{Q}^{\mathcal{N}}} \frac{r_N^p(q;\boldsymbol{\mu})}{\|q\|_{\mathcal{Q}}}$$

are the dual norms of the residuals for the velocity and the pressure variables, respectively, such that $\|r_N(\cdot;\boldsymbol{\mu})\|_{\mathcal{Y}'}^2 = \|r_N^v(\cdot\,;\boldsymbol{\mu})\|_{\mathcal{X}'}^2 + \|r_N^p(\cdot\,;\boldsymbol{\mu})\|_{\mathcal{Q}'}^2$. Efficient and reliable methods of computing both the dual norm of the residual and the lower bound $\beta_{LB}(\boldsymbol{\mu})$ are presented in [36].

5.3. *Offline-Online computational strategy*

A suitable Offline/Online decomposition stratagem enables to decouple the generation and projection stages of the RB approximation. In an expensive Offline stage we prepare a very small RB "database", while in the Online stage, for each new value of $\boldsymbol{\mu} \in \mathcal{D}$, we rapidly evaluate both the output of interest and the associated a posteriori error bound whose complexity is independent of the dimension $\mathcal{N}$ of the "truth" FE approximation space. The possibility to handle with this computational procedure is based on an affine parametric dependence assumption on both bilinear and linear forms. If the mapping $T(\cdot;\boldsymbol{\mu}) : \Omega \to \Omega_o(\boldsymbol{\mu})$ is affine, parametric bilinear forms $a(\cdot,\cdot;\boldsymbol{\mu})$ and $b(\cdot,\cdot;\boldsymbol{\mu})$ are affinely parametrized [31, 37], i.e.

$$a(\mathbf{v},\mathbf{w};\boldsymbol{\mu}) = \sum_{q=1}^{Q_a} \Theta_a^q(\boldsymbol{\mu}) a^q(\mathbf{v},\mathbf{w}), \qquad b(p,\mathbf{w};\boldsymbol{\mu}) = \sum_{q=1}^{Q_b} \Theta_b^q(\boldsymbol{\mu}) b^q(p,\mathbf{w}) \tag{29}$$

for some integers Q_a, Q_b, where q is a condensed index for (i,j,k), and as done in [40]

$$a^{q(i,j,k)}(\mathbf{v},\mathbf{w}) = \int_\Omega \xi_k^{i,j}(\mathbf{x}) \frac{\partial \mathbf{v}}{\partial x_i} \frac{\partial \mathbf{w}}{\partial x_j} d\Omega, \quad b^{q(i,j,k)}(p,\mathbf{w}) = -\int_\Omega \eta_k^{i,j}(\mathbf{x}) p \frac{\partial \mathbf{w}_i}{\partial x_j} d\Omega, \tag{30}$$

$$\Theta_a^q(\boldsymbol{\mu}) = \beta_k^{i,j}(\boldsymbol{\mu}), \qquad \Theta_b^q(\boldsymbol{\mu}) = \gamma_k^{i,j}(\boldsymbol{\mu}),$$

DOI: 10.1002/fld

$$\nu_{ij}(\mathbf{x},\boldsymbol{\mu}) = \sum_{k=1}^{K_{ij}^a} \beta_k^{i,j}(\boldsymbol{\mu})\xi_k^{i,j}(\mathbf{x}), \qquad \chi_{ij}(\mathbf{x},\boldsymbol{\mu}) = \sum_{k=1}^{K_{ij}^b} \gamma_k^{i,j}(\boldsymbol{\mu})\eta_k^{i,j}(\mathbf{x}), \qquad 1 \le i,j \le 2. \tag{31}$$

where K_{ij}^a and K_{ij}^b represent the total number of terms obtained for each tensorial component after the empirical interpolation procedure. In the same way, we can write the right-hand-side terms as

$$\langle F^s, \mathbf{w}\rangle + \langle F^l, \mathbf{w}\rangle = \sum_{q=1}^{Q_F+Q_a} \Theta_q^F(\boldsymbol{\mu})F^q(\mathbf{w}), \qquad \langle G, \phi\rangle = \sum_{q=1}^{Q_G} \Theta_q^G(\boldsymbol{\mu})G^q(\phi) \tag{32}$$

for some integers Q_F and $Q_G \equiv Q_b$, where here q is a condensed index for (i,k),

$$F^q(\mathbf{w}) = \int_\Omega \psi_k^i(\mathbf{x})\mathbf{w}_i d\Omega, \qquad \Theta_q^F(\boldsymbol{\mu}) = \delta_k^i(\boldsymbol{\mu}), \qquad q = 1,\dots,Q_F, \tag{33}$$

$$f_i(\mathbf{x})|\det J_T(\mathbf{x},\boldsymbol{\mu})| = \sum_{k=1}^{K_i^f} \delta_k^i(\boldsymbol{\mu})\psi_k^i(\mathbf{x}), \qquad i = 1,2, \tag{34}$$

$$\begin{aligned} F^q(\mathbf{w}) &= a^q(R\mathbf{v}_g,\mathbf{w}), \quad \Theta_q^F(\boldsymbol{\mu}) = -\Theta_q^a(\boldsymbol{\mu}), \qquad q = Q_F+1,\dots,Q_F+Q_a, \\ G^q(\phi) &= b^q(\phi,R\mathbf{v}_g), \quad \Theta_q^G(\boldsymbol{\mu}) = -\Theta_q^b(\boldsymbol{\mu}), \qquad q = 1,\dots,Q_G = Q_b. \end{aligned} \tag{35}$$

Under these assumptions, solution of (26) can be split into Offline and Online stages, being

$$\begin{cases} \displaystyle\sum_{q=1}^{Q_a} \Theta_a^q(\boldsymbol{\mu})a^q(\mathbf{v}_N^{\mathcal{N}}(\boldsymbol{\mu}),\mathbf{w}) + \sum_{q=1}^{Q_b} \Theta_b^q(\boldsymbol{\mu})b^q(p_N^{\mathcal{N}}(\boldsymbol{\mu}),\mathbf{w}) = \sum_{q=1}^{Q_F+Q_a} \Theta_q^F(\boldsymbol{\mu})F^q(\mathbf{w}) \\ \displaystyle\sum_{q=1}^{Q_b} \Theta_b^q(\boldsymbol{\mu})b^q(q,\mathbf{v}_N^{\mathcal{N}}(\boldsymbol{\mu})) = \sum_{q=1}^{Q_G} \Theta_q^G(\boldsymbol{\mu})G^q(\phi) \end{cases} \tag{36}$$

for all $\mathbf{w} \in \mathcal{X}_N^{\mathcal{N}}$, $\phi \in \mathcal{Q}_N^{\mathcal{N}}$. Using the expressions (27), system (36) becomes, componentwise,

$$\begin{cases} \displaystyle\sum_{j=1}^{2N}\sum_{q=1}^{Q_a} \Theta_a^q(\boldsymbol{\mu})A_{ij}^q v_{Nj}(\boldsymbol{\mu}) + \sum_{l=1}^{N}\sum_{q=1}^{Q_b} \Theta_b^q(\boldsymbol{\mu})B_{il}^q p_{Nl}(\boldsymbol{\mu}) = \sum_{q=1}^{Q_F+Q_a} \Theta_q^f(\boldsymbol{\mu})F_i^q, & 1 \le i \le 2N \\ \displaystyle\sum_{j=1}^{2N}\sum_{q=1}^{Q_b} \Theta_b^q(\boldsymbol{\mu})B_{jl}^q v_{Nj}(\boldsymbol{\mu}) = \sum_{q=1}^{Q_G} \Theta_q^g(\boldsymbol{\mu})G_l^q, & 1 \le l \le N \end{cases} \tag{37}$$

where $A_{ij}^q = a^q(\sigma_j,\sigma_i)$, $B_{il}^q = b^q(\zeta_l,\sigma_i)$, $F_i^q = \mathbf{f}^q(\sigma_i)$ and $G_l^q = g^q(\zeta_l)$. In this way, computation entails an expensive $\boldsymbol{\mu}$-independent Offline stage performed only once and an Online stage for any chosen parameter value $\boldsymbol{\mu} \in \mathcal{D}$. During the former the basis functions σ_n, ζ_l, the matrices A^q, B^q and the vectors F^q, G^q are computed and stored; in the latter, for any given $\boldsymbol{\mu}$, all the $\Theta_q(\boldsymbol{\mu})$ coefficients are evaluated and then the $3N \times 3N$ linear system (37) is assembled and solved as a usual Stokes system, being of the form

$$\begin{pmatrix} A & B \\ B^T & 0 \end{pmatrix} \begin{pmatrix} v_N \\ p_N \end{pmatrix} = \begin{pmatrix} F \\ G \end{pmatrix}. \tag{38}$$

DOI: 10.1002/fld

Although being dense (rather than sparse as in the FE case), the system matrix is very small, with a size independent of the FE space dimension $\mathcal{N}$. Details about the assembling procedure of these matrices will be given in the next section. Moreover, also the dual norm of the residual appearing in (28) can be computed efficiently by using the Offline-Online procedure [31, 37]. Since the map $T(\cdot;\boldsymbol{\mu})$ (22) obtained by FFD method is a polynomial map, the tensor $\boldsymbol{\nu}_T(\mathbf{x};\boldsymbol{\mu})$ is not affinely parametrized in the sense of (31). Hence, an intermediate step is necessary in order to recover the affinity assumption and thus the possibility of computing the RB solution through an Offline/Online decomposition. In the nonaffine case, we rely on the empirical interpolation method (EIM) [4, 15], which is an interpolation method for parametric functions based on adaptively chosen interpolation points and global shape functions. According to EIM, each component $\nu_{ij}(\mathbf{x};\boldsymbol{\mu})$ is approximated by an affine expansion

$$\tilde{\nu}_{i,j}(\mathbf{x};\boldsymbol{\mu}) = \sum_{k=1}^{K_{ij}^a} \tilde{\beta}_k^{i,j}(\boldsymbol{\mu})\tilde{\xi}_k^{i,j}(\mathbf{x}) + \varepsilon_{i,j}^a(\mathbf{x};\boldsymbol{\mu}). \tag{39}$$

The same approximation is set up for $\boldsymbol{\chi}_T$ and the right-hand-side of velocity equation:

$$\begin{aligned} \tilde{\chi}_{i,j}(\mathbf{x};\boldsymbol{\mu}) &= \sum_{k=1}^{K_{ij}^b} \tilde{\gamma}_k^{i,j}(\boldsymbol{\mu})\tilde{\eta}_k^{i,j}(\mathbf{x}) + \varepsilon_{i,j}^b(\mathbf{x};\boldsymbol{\mu}), \\ f_i(\mathbf{x})|\det(J_T(\mathbf{x};\boldsymbol{\mu}))| &= \sum_{k=1}^{\tilde{K}_i^f} \tilde{\delta}_k^i(\boldsymbol{\mu})\tilde{\psi}_k^i(\mathbf{x}) + \varepsilon_i(\mathbf{x};\boldsymbol{\mu}). \end{aligned} \tag{40}$$

All the coefficients $\beta_k^{i,j}$'s, $\gamma_k^{i,j}$'s, δ_k^i's, $\xi_k^{i,j}$'s, $\eta_k^{i,j}$'s and ψ_k^i's are efficiently computable scalar functions and the error terms are guaranteed to be under some tolerance,

$$\|\varepsilon_{i,j}^{(a,b)}(\cdot;\boldsymbol{\mu})\|_\infty \leq \varepsilon_{tol}^{EIM}, \quad \|\varepsilon_i(\cdot;\boldsymbol{\mu})\|_\infty \leq \varepsilon_{tol}^{EIM}, \quad \forall \boldsymbol{\mu} \in \mathcal{D}.$$

We refer the reader to [4, 29] for details on EIM procedures for non-affine RB problems and to [23] for details on its application in the FFD context introduced in Sec. 4.

6. NUMERICAL PROCEDURE FOR REDUCED SHAPE OPTIMIZATION

We present in this section the numerical procedure implemented for the solution of the reduced shape optimization problem (8), which is a nonlinear programming problem but depending on a relatively small number of parameters. It can be solved in a very efficient way by means of a suitable combination of the techniques analyzed in the previous sections – RB methods, shape parametrization by FFD techniques and EIM for treating non-affinities. In more details, upgrading the procedure of [23] to the case of viscous flows:

1. *Shape parametrization*. Select a shape parametrization technique, input parameters $\mu_1, \ldots, \mu_p$ and the parameter set $\mathcal{D}$ on the basis of problem-dependent criteria.

DOI: 10.1002/fld

2. *Parametrized formulation*. Compute the map $T(\cdot;\boldsymbol{\mu})$ and the tensors $\boldsymbol{J}_T(\boldsymbol{\mu})$, $\boldsymbol{\nu}(\boldsymbol{\mu})$ and $\boldsymbol{\chi}(\boldsymbol{\mu})$ in order to get the parametrized formulation (5). The transformation tensors (14) and (15) are computed symbolically by means of a Computer Algebra System (CAS).
3. *Empirical interpolation*. Compute the affine expansions (31)-(34) in case of nonaffinely parametrized tensors by applying the EIM procedure to each tensor component.
4. *FE structures*. Assemble FE structures corresponding to the $\boldsymbol{\mu}$-independent terms of (29)-(32), using the affine expansions of the tensors computed at point 3. In particular, assemble the matrices $\mathcal{A}^q \in \mathbb{R}^{\mathcal{N}_X \times \mathcal{N}_X}$ $(q = 1, \ldots, Q_a)$, $\mathcal{B}^q \in \mathbb{R}^{\mathcal{N}_X \times \mathcal{N}_Q}$ $(q = 1, \ldots, Q_b)$ corresponding to the bilinear forms (30) and the right-hand sides $\mathcal{F}^q \in \mathbb{R}^{\mathcal{N}_X}$ $(q = 1, \ldots, Q_F)$, $\mathcal{G}^q \in \mathbb{R}^{\mathcal{N}_Q}$ $(q = 1, \ldots, Q_G)$ corresponding to the linear forms (33) and (35).
5. *Inf-sup constant lower bound*. By means of the *successive constraint method* (SCM) [36] compute the structures for the lower bound of the inf-sup constant $\beta_{LB}^{\mathcal{N}}(\boldsymbol{\mu})$.
6. *RB space construction*. Perform the *greedy* procedure presented in Sec. 5.2 for building the RB spaces $\mathcal{X}_N^{\mathcal{N}}$ and $\mathcal{Q}_N$ for velocity and pressure respectively. For each selected $\boldsymbol{\mu}^n$, the corresponding Stokes problem has been solved using the *Pressure-Matrix Method*; moreover, at each iteration the space $\mathcal{X}_N$ is enriched by the solution of (24) (supremizer operator) and a Gram-Schmidt ortonormalization is executed.
7. *RB post-processing*. After the *greedy* basis selection procedure, matrices A^q, B^q and vectors F^q, G^q are obtained by a pre- and post- multiplication of the corresponding FE structures with the RB representations $\mathcal{Z}_X = [\,\boldsymbol{\sigma}_1 \,|\, \ldots \,|\, \boldsymbol{\sigma}_{2N}\,]$, $\mathcal{Z}_Q = [\,\zeta_1 \,|\, \ldots \,|\, \zeta_N\,]$:

$$A^q = \mathcal{Z}_X^T \mathcal{A}^q \mathcal{Z}_X, \quad q = 1, \ldots, Q_a; \qquad B^q = \mathcal{Z}_X^T \mathcal{B}^q \mathcal{Z}_X, \quad q = 1, \ldots, Q_b;$$
$$F^q = \mathcal{Z}_X^T \mathcal{F}^q, \quad q = 1, \ldots, Q_a + Q_F; \qquad G^q = \mathcal{Z}_Q^T \mathcal{G}^q, \quad q = 1, \ldots, Q_G \equiv Q_b.$$

At this point, the *Offline* preparation[b] is completed. Then, we perform the

8) *Numerical Optimization*. Solve the optimization problem by a suitable optimization subroutine; at each step, an *Online* evaluation of RB solution and output is requested. The optimization procedure stops when the (approximated) gradient of the cost functional is under a very small tolerance ε_{tol}^{OPT}.

The *Offline* stage thus depends on the choice of the FE spaces (whose dimension is $\mathcal{N}_{\mathcal{X}} + \mathcal{N}_{\mathcal{Q}}$), the reference domain Ω and the FFD structure. For the RB Offline computations we have used the `rbMIT` library [21,31], while for the FE assembling stage we have exploited the `MLife` library [41], enhanced in `Matlab`-PDE toolbox environment.
The *Online* stage consists of many evaluations of field variables $(\mathbf{v}_N(\boldsymbol{\mu}), p_N(\boldsymbol{\mu}))$ and parametric output $s_N(\boldsymbol{\mu})$, as required by the optimization procedure; in our case, the optimization problem has been solved using the sequential quadratic programming (SQP) algorithm, see e.g. [20].

[b] Efficient and reliable methods of computing both the dual norm of the residual and lower bounds $\beta_{LB}^{\mathcal{N}}(\boldsymbol{\mu})$ are used in order to exploit the *Offline-Online* computational stratagem also for the error estimation.

Prepared using fldauth.cls
DOI: 10.1002/fld

7. NUMERICAL RESULTS

Let us now present the results for the bypass problem obtained through the reduced shape optimization strategy discussed in the previous sections. Two different cases have been analyzed, considering different blockage conditions in the occluded coronary artery, since a residual blood flow in this vessel implies different vorticity profiles in the downfield region. In Case A a completely occluded coronary is considered, corresponding to setting $\mathbf{g}^D = \mathbf{0}$ on Γ_a, while in Case B a partially stenosed coronary is considered, choosing a residual horizontal flux given by $\mathbf{g}^D = (\max(\tilde{v}_0 \exp(-(x - x_M)^2/\beta) - \omega, 0), 0)$ on Γ_a, where x_M is the middle point of side Γ_a and $\beta = 10^{-3}$, $\omega = 10^{-1}$ are constants which model the patency of the stenosis; here we consider a residual flow rate of about 15% of the one in the bypass grafting.

In both cases, the same reference configuration Ω, depicted in Fig. 4, has been chosen similar to some bypass configurations already considered in previous works [25,33,34], fixing the observation subregion $\Omega_{df} = \{\mathbf{x} = (x_1, x_2) \in \Omega : x_1 > 1.5\}$. The FFD parametrization has been built on a 5×6 lattice of control points on the rectangle $D = [-1, 3] \times [-0.6, 0.4]$, for a total number of 60 degrees of freedom; $P = 8$ of these degrees of freedom have been selected as design variables, given by seven vertical and one horizontal deformations. Previous analysis on the shape of an aorto-coronaric bypass [11, 34, 45] have highlighted an important dependence of the blood flow on the *anastomotic angle* between the incoming branch of the graft and the artery, and on the ratio between the diameters of these two branches; our selected design variables thus aim at controlling shape variations in this sense. In particular, parameters μ_3 and μ_5 (the latter is the only one giving an horizontal deformation) control the anastomotic angle, parameters μ_6 and μ_8 control the diameters ratio (see Fig. 4). Moreover, parameters μ_4 and μ_7 control the upper shape of the anastomotic bifurcation, while μ_1 and μ_2 are responsible of the shape of the lower wall, which has to be curved since it is positioned on the heart wall. The parametric domain $\mathcal{D}$ is therefore given by

$$\mathcal{D} = \{\boldsymbol{\mu} = (\mu_1, \ldots, \mu_8) \in \mathbb{R}^8 : \ \mu_i \in [-0.2, 0.2] \ \ \forall\, i \neq 5, \ \mu_5 \in [0, 1]\}.$$

The number of parameters $P = 8$ has been selected to ensure a trade-off between *(i)* a significative shape versatility during the optimization process and *(ii)* a better computational performance at each iteration of the optimization process[c]. The points location (and their activation) have been emphasized in sensible zone of the bypass [1, 34]. The ranges of variation of the control points positions with respect to the original locations ensure to keep small deformations.

Reduced basis approximation have been built upon a finite element approximation on $\mathbb{P}^2 - \mathbb{P}^1$ spaces of dimension $\mathcal{N}_X = 33,330$ and $\mathcal{N}_Q = 4,269$ respectively, obtained on a non-conforming mesh of $8,128$ triangular elements. In particular, since FFD and EIM steps depend just on the geometric map, they can be performed only once for both cases A and B. In both cases, by setting $\varepsilon_{tol}^{EIM} = 2.5 \times 10^{-4}$, we obtain an effine expansion of $\sum_{i,j} \tilde{K}_{ij}^a = 204$ terms for $\tilde{\nu}_{ij}$ components, of $\sum_{i,j} \tilde{K}_{ij}^b = 18$ terms for $\tilde{\chi}_{ij}$ components and of $\sum_i \tilde{K}_i^f = 5$ terms for the right hand-side

[c]By reducing the number of parameters (for example to $P = 6$ and at the same time by increasing their range of variation may give the same effect as augmenting the number of parameters (for example to $P = 10$) and reducing their range of variation. The difference between these two alternatives is mainly due to computational difficulties occurring in the certification for the first case and in the Online efficiency for the second one.

DOI: 10.1002/fld

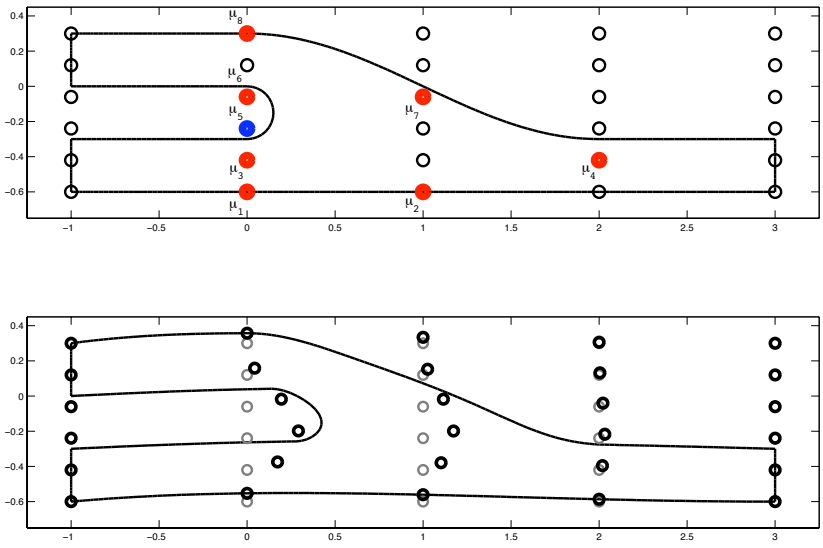

Figure 4. Top: reference domain Ω and FFD setting. Control points depicted in red/black can be freely moved in vertical/horizontal direction. Bottom: an example of shape deformation; grey points correspond to the undeformed shape ($\boldsymbol{\mu} = \mathbf{0}$), black ones to a selected value of $\boldsymbol{\mu} \neq \mathbf{0}$.

components; see Fig. 5 for an example of tensor reconstruction through EIM.

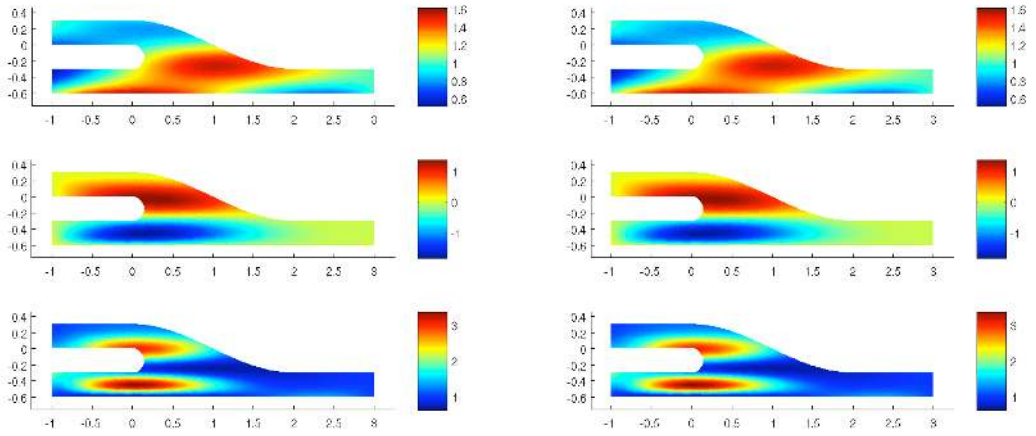

Figure 5. Tensor components $\nu_{1,1}(\mathbf{x};\bar{\boldsymbol{\mu}})$, $\nu_{1,2}(\mathbf{x};\bar{\boldsymbol{\mu}}) \equiv \nu_{2,1}(\mathbf{x};\bar{\boldsymbol{\mu}})$, $\nu_{2,2}(\mathbf{x};\bar{\boldsymbol{\mu}})$ on Ω for a randomly chosen $\bar{\boldsymbol{\mu}} \in \mathcal{D}$ (left) and corresponding affine reconstructions obtained by empirical interpolation (right).

Instead, the assembling of FE structures, the estimation of the inf-sup constant lower bound and the *greedy* algorithm for snapshots selection have to be done separately, once for each case. In particular, tolerances for RB *greedy* algorithm ε_{tol}^{RB} and empirical interpolation ε_{tol}^{EIM} are chosen such that the error on EIM is kept under the error on RB construction.

With $\varepsilon_{tol}^{RB} = 5 \cdot 10^{-4}$, $N = 21$ and $N = 20$ basis functions have been selected for case A and B,

DOI: 10.1002/fld

giving RB spaces of total dimension 63 and 60, respectively. Moreover, a tolerance $\varepsilon_{tol}^{OPT} = 10^{-6}$ has been chosen for the stopping criterium of the optimization procedure, based on the magnitude of the (approximated) gradient of the cost functional.

In Fig. 6 we report the certification of the RB approach by a posteriori error estimation presented in [36] and its comparison with true error; in Fig. 7 we report the error $\|s^{\mathcal{N}}(\boldsymbol{\mu}) - s_N(\boldsymbol{\mu})\| = \|\mathcal{J}(\mathbf{v}^{\mathcal{N}}(\boldsymbol{\mu})) - \mathcal{J}(\mathbf{v}_N(\boldsymbol{\mu}))\|$ between the FE and the RB approximations of the vorticity output (20). In both cases, errors and error bounds have been evaluated on a uniform sample $\Xi \subset \mathcal{D}$ of size $|\Xi| = 1000$.

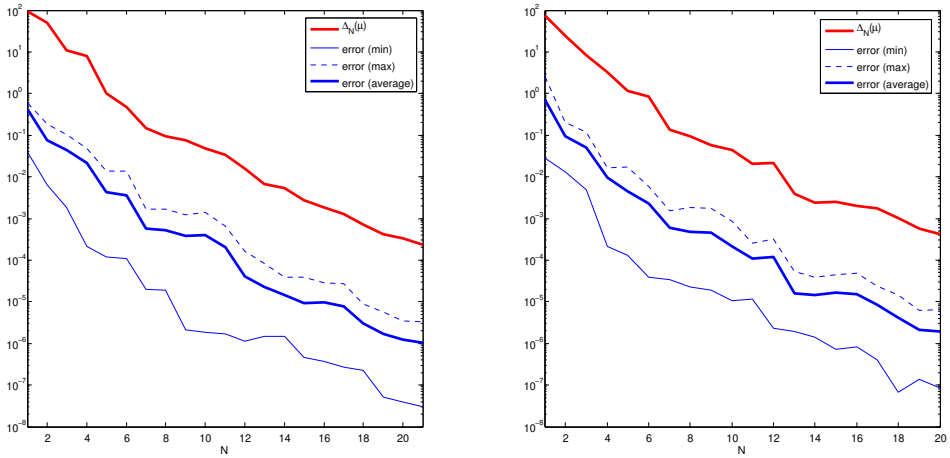

Figure 6. A posteriori error bounds and (minimum, maximum and average) computed errors between the "truth" FE solution and the RB approximation for test case A (left) and B (right).

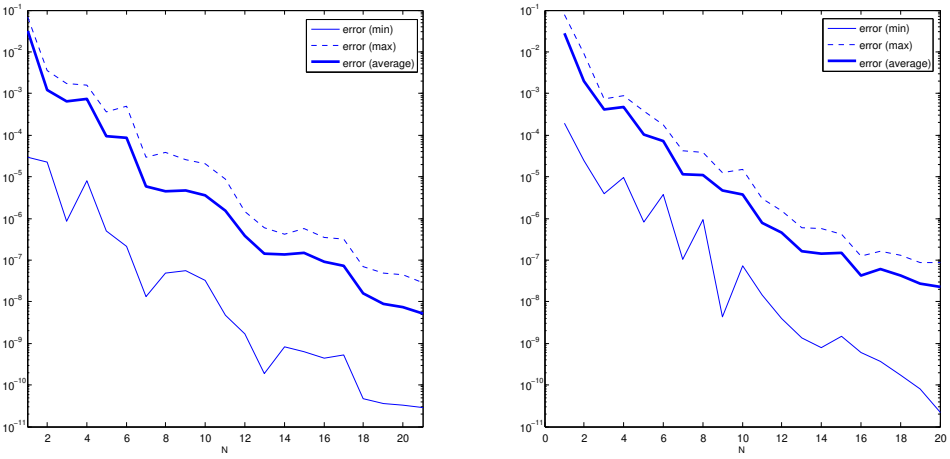

Figure 7. Minimum, maximum and average computed errors on the vorticity output between the "truth" FE solution and the RB approximation for test case A (left) and B (right).

DOI: 10.1002/fld

7.1. Modelling aspects

For the test case A, a vorticity reduction of about 39% has been obtained through the described procedure; the cost functional decreases from an initial value $s_N(\boldsymbol{\mu}^{(0)}) = 459.40$ to an optimal value $s_N(\hat{\boldsymbol{\mu}}_{RB}) = 281.25$ after 36 optimization steps performed in $2968s$ until convergence[d].
In Fig. 8 the reference and the optimal configurations are displayed, together with deformation induced by the displacement of the control points. Flow variables and corresponding vorticity layers for the initial and the optimal configurations are represented in Fig. 9.

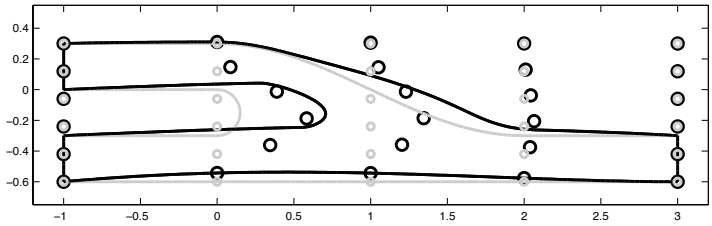

Figure 8. Test A: reference configuration (in grey), optimal shape (in black) and corresponding control points displacement.

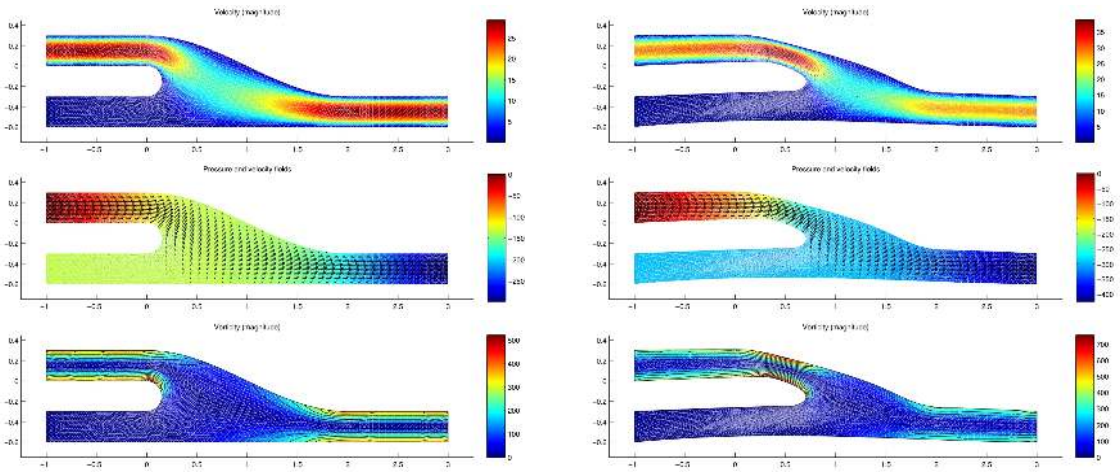

Figure 9. Test A: velocity field, pressure field and vorticity magnitude for the reference (left) and the optimal (right) configuration.

For the test case B, a vorticity reduction of about 45% has been obtained, passing from an initial value of the cost functional $s_N(\boldsymbol{\mu}^{(0)}) = 839.45$ to an optimal value of $s_N(\hat{\boldsymbol{\mu}}_{RB}) = 466.05$ after 45 optimization steps, which have been performed in $3554s$. Optimal configuration obtained in this case is displaied in Fig. 10, while flow variables and the corresponding vorticity layers for the initial and the optimal configurations are represented in Fig. 11.

The results of the analysis performed in this work show that graft anastomosis configurations play an important role in the pattern of the flow and the distribution of the vorticity generated

[d]Computations have been executed on a personal computer with 2×2GHz Dual Core AMD Opteron (tm) processors 2214 HE and 16 GB of RAM.

DOI: 10.1002/fld

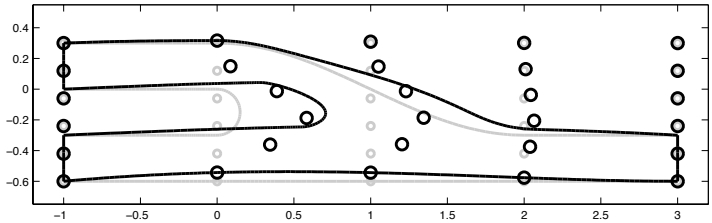

Figure 10. Test B: reference configuration and optimal shape with corresponding control points displacement.

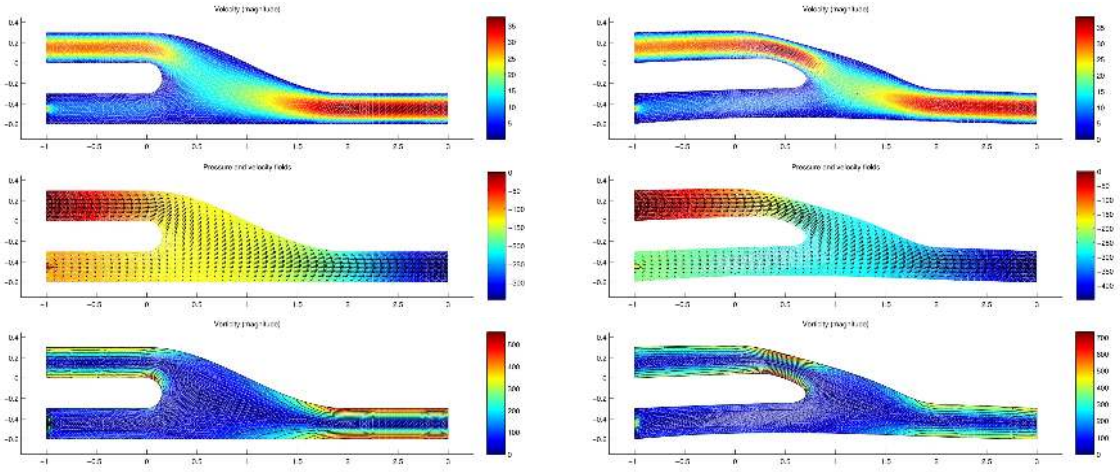

Figure 11. Test B: velocity field, pressure field and vorticity magnitude for the reference (left) and the optimal (right) configuration.

downstream. A remarkable observation is that – even if the optimal shape are quite similar – the magnitude of the vorticity on the anastomosis highly depends on the presence of a residual patency in the obstructed host coronary artery; in particular, in the down field region vorticity magnitude is higher whether a residual flow is present. In both cases, the iteratively optimized geometry has a much smoother toe and heel than the initial shape; optimal shapes also show smoother curvatures at the heel with a gradual transition in the toe region, as already pointed out in the work by Lei et al. [25]. The localization of maximum values of vorticity at the heel and toe is expected, because this is the region where disturbed flows occur, even with a Stokes model; the same conclusion can be drawn for wall shear stress gradient and Navier-Stokes flows [25]. Moreover, higher values in the heel region are not as clinically significant as the high vorticity values near the toe region and in the down-field region, which is a well-known location where restenosis might reform.

The shape optimization procedure however enables to reduce the vorticity in the down-field region of the anastomosis, even if increasing values of vorticity arise at heel and top segments. In the case where the observation region Ω_{obs} is the whole domain Ω instead of the subdomain Ω_{df} – and thus vorticity is minimized all over the anastomosis – different results can be obtained, both in terms of optimal shapes and vorticity reduction. By using the same procedure as before, we obtain (e.g. for test case B) the vorticity patterns in Fig. 12: the minimization of the vorticity all over the anastomosis leads to optimal shapes characterized by bigger sections and narrow bifurcations. Moreover, the parameter μ_5 – which strongly affects the anastomotic angle – seems to play an important role in

DOI: 10.1002/fld

the behavior of the vorticity field. For both test cases numerical results are summarized in Tabs. I and II.

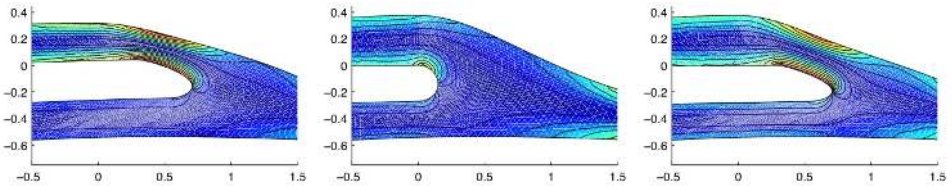

Figure 12. Test B: optimal shapes (and related vorticity patterns) obtained through vorticity minimization on the down-field region Ω_{df} (left) and on the whole domain Ω (middle, right). In the third case the parameter μ_5 has been fixed equal to the optimal value obtained in the first case by vorticity minimization on Ω_{df}.

Ω_{obs}	$s_N(\boldsymbol{\mu}^{(0)})$	$s_N(\hat{\boldsymbol{\mu}}_{RB})$	Δs_N	# iterations	cpu (s)
Ω_{df}	459.40	281.25	38.8%	36	2968
Ω	844.93	576.75	31.7%	45	3504

Table I. Test case A: initial and optimal value of cost functional, total reduction, number of iterations of the optimization procedure and cpu times for a vorticity observation on Ω_{df} and Ω.

Ω_{obs}	$s_N(\boldsymbol{\mu}^{(0)})$	$s_N(\hat{\boldsymbol{\mu}}_{RB})$	Δs_N	# iterations	cpu (s)
Ω_{df}	839.45	466.05	44.5%	45	3554
Ω	1492.5	934.25	37.4%	158	10492

Table II. Test case B: initial and optimal value of cost functional, total reduction, number of iterations of the optimization procedure and cpu times for a vorticity observation on Ω_{df} and Ω.

We also compare the results of the downfield vorticity minimization problem based on the reduced (basis) procedure with the ones obtained using the truth FE approximation of the Stokes flow (see Tab. III). In the considered cases, the solution of the reduced optimization problem $s_N(\hat{\boldsymbol{\mu}}_{RB})$ shows a slight difference (less than 0.1% in the output value) and results sub-optimal with respect to the solution $s_{\mathcal{N}}(\hat{\boldsymbol{\mu}}_{FE})$ computed by using the truth FE approximation; this fact has already been remarked both in an optimal control [12] and in a shape optimization [23] context.

	Case A	Case B
$s_N(\hat{\boldsymbol{\mu}}_{RB})$	281.25	466.05
$s_{\mathcal{N}}(\hat{\boldsymbol{\mu}}_{FE})$	281.17	465.89
$\frac{\lvert s_N(\hat{\boldsymbol{\mu}}_{RB}) - s_{\mathcal{N}}(\hat{\boldsymbol{\mu}}_{FE})\rvert}{s_{\mathcal{N}}(\hat{\boldsymbol{\mu}}_{FE})}$	$3 \cdot 10^{-4}$	$3 \cdot 10^{-4}$

Table III. Optimal values of cost functional (downfield vorticity, $\Omega_{obs} = \Omega_{df}$) for the optimization based on RB and FE approximations, for test cases A and B.

DOI: 10.1002/fld

7.2. *Feedback validation by "high-fidelity" model*

Another important feedback is provided by the comparison of the results obtained by using a "low-fidelity" Stokes model for the blood flow with the Navier-Stokes flows computed on the same shape configurations. We consider the initial shape and the optimal shape obtained by minimizing the blood vorticity corresponding to the Stokes flow, in both cases A and B. We then compute the Navier-Stokes flows and vorticity distributions corresponding to the same configuration and boundary conditions. We obtain in this case a vorticity reduction in the downfield region Ω_{obs} of 39.9% in case A and of 44.5% in case B, respectively – which slightly differs from the reduction obtained by using a Stokes model. Moreover, in the four considered configurations (initial and optimal shapes for cases A and B) the difference between the computed vorticity outputs $s_N(\cdot)$ and $s_N^{NS}(\cdot)$ is smaller than 5% (see Tab. IV). Clearly, in the Navier-Stokes case velocity fields are influenced by the presence of the (nonlinear) convective term. This feedback is provided with the sole aim of testing with a higher-fidelity fluid model the optimal shape obtained with the low-fidelity model. Nevertheless, we can consider this shape *optimal* only for the Stokes model and just *optimized* for the Navier-Stokes model. Previous feedback results were provided in [33]. We report in Fig. 13 the velocity and the vorticity fields computed on the optimal configurations in cases A and B.

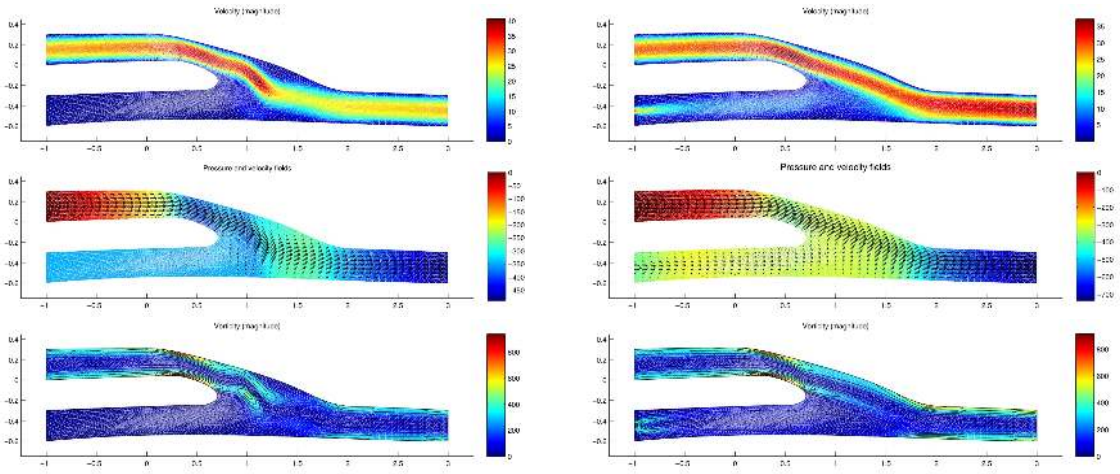

Figure 13. Feedback validation: velocity, pressure and vorticity fields computed by using a Navier-Stokes model in the optimal configuration of cases A (left) and B (right).

	Stokes case	Navier-Stokes case
case A	$s_N(\boldsymbol{\mu}^{(0)}) = 459.40$	$s_N^{NS}(\boldsymbol{\mu}^{(0)}) = 469.14$
	$s_N(\hat{\boldsymbol{\mu}}_{RB}) = 281.25$	$s_N^{NS}(\hat{\boldsymbol{\mu}}_{RB}) = 281.81$
case B	$s_N(\boldsymbol{\mu}^{(0)}) = 839.45$	$s_N^{NS}(\boldsymbol{\mu}^{(0)}) = 878.32$
	$s_N(\hat{\boldsymbol{\mu}}_{RB}) = 466.05$	$s_N^{NS}(\hat{\boldsymbol{\mu}}_{RB}) = 488.50$

Table IV. Feedback validation (downfield vorticity minimization): cost functional values for initial and optimal configurations computed with a Stokes and a Navier-Stokes flow model.

DOI: 10.1002/fld

7.3. Computational features

Reduced basis techniques, combined with a free-form deformation framework for shape optimization, allow a substantial reduction of both geometrical complexity and computational work. An iterative optimization procedure is greatly enhanced by the computational gain since at each step the cost functional to be minimized is evaluated using the RB approximation. Compared to a flow simulation by finite elements, in our 2D aorto-coronaric bypass case, a RB Online evaluation of flow variables enables a computational speedup of about 100 times. In particular, the average time over 100 Online evaluations is of $t_{RB}^{online} = 2.204$ seconds for the test case A and of $t_{RB}^{online} = 2.012$ seconds for the test case B, while the corresponding FE computations take an average time of $t_{FE} = 209$ and $t_{FE} = 216$ seconds, respectively. More details are reported in Tab. V. This is basically due to the reduction of about 500 times in the dimension of the linear systems obtained by finite element discretization and reduced basis approximation: in the first case, we get a sparse linear system of dimension $35,997$ while in the second case linear systems – which are now of full type – have dimension 72 and 66, for the test case A and B, respectively. Consequently, computational times for the whole optimization process are reduced too, depending almost linearly by the time for a single Online evaluation.

Moreover, a shape parametrization based on FFD allows a strong reduction in geometrical complexity: indeed, geometrical reduction in term of the number of parameters is of about 100 with respect to traditional shape parametrization based on local boundary variation. However, by acting on a small set of design variables it is possible to describe a wide family of shapes and thus perform optimization in a low dimensional but quite rich space of admissible configurations. On the one hand, by properly choosing the location of the parameters, FFD enables not to constrain *a priori* the shape of a configuration too similar with respect to the initial one, as in the case where affine or non-affine mappings on different subdomains are used [34, 35], and make the upper wall free to deform; on the other hand, it allows a strict control on those parts where a shape is in some sense prescribed (as in the case of the lower wall). In the end, we take into account also the time spent for the Offline construction and storage; this allows to determine the break-even point, given by $\mathcal{Q}_{BE} = t_{RB}^{offline}/t_{FE}$. In particular, we obtain a break-even point of $\mathcal{O}(10^2)$ in both cases. Note that Offline procedures for basis assembling and certification of the error are the same even if we change the cost functional or the optimization goal: in this way Offline efforts can be reused for different Online optimization procedures.

	FE	RB (min)	RB (average)	RB (max)	Speedup
Test Case A	209.06s	1.939s	2.012s	3.078s	94.85
Test Case B	215.76s	1.945s	2.204s	3.314s	107.18

Table V. Computational times and speedup for reduced basis Online evaluations and finite element computations. RB Online evaluations have been executed considering a sample of 100 randomly chosen parameter vectors $\boldsymbol{\mu} \in \mathcal{D}$.

DOI: 10.1002/fld

8. CONCLUSIONS AND FURTHER DEVELOPMENTS

The purpose of the present work has been to develop a model order reduction strategy for shape optimization by coupling reduced basis methods for flow simulation with free-form deformation techniques for shape parametrization. This framework has been applied to an optimal design problem of an aorto-coronaric bypass anastomosis, allowing a substantial reduction in both computational efforts (w.r.t. classical strategies based on finite element discretization techniques) and geometrical complexity (w.r.t. more traditional shape parametrization approaches). A reduced basis formulation has been discussed for noncoercive problems, taking advantage of the empirical interpolation method to deal with the nonaffine parametric dependence. A free-form deformation setting has been presented and applied to a complex 2D configuration. The combination of several reduction techniques allows the treatment of more complex and versatile geometrical parametrizations, to keep under control the number of parameters and to achieve significant computational savings.

For more realistic investigations, the extension of this framework to Navier-Stokes equations and 3D configurations is in order and represents our current research activity. The accuracy of future simulations and optimization stages is dependent on the acquisition of patient-specific data such as geometry properties or flow conditions [26]. Following this path, we intend to consider in the next future a coupled parametrization of both geometrical and flow physical properties, such as blood rheology or boundary conditions. Moreover, an efficient characterization of a posteriori error estimators for quadratic output is currently under investigation.

APPENDIX A - BYPASS SURGERY: MEDICAL AND BIO-ENGINEERING ASPECTS

Aorto-coronaric bypass graft surgery represents the standard treatment of advanced coronary arteries diseases. Coronaries allow the circulation of blood in vessels of the heart muscle; in particular, coronary arteries deliver oxygen-rich blood to the myocardium. In fact, when a coronary artery is affected by atheromatous plaques or a stenosis, the heart muscle does not receive the necessary oxygen amount through blood circulation: aorto-coronaric anastomosis thus restores oxygenation through a bypass surgery downstream an occlusion (see Fig. 14).

Different kinds and shapes for aorto-coronaric bypass anastomoses are available, such as Miller cuffed models, Taylor patches, etc. Consequently, different surgery procedures are used to set up a bypass; in general, the connection of the graft to the coronary artery can be done using an end-to-side or a side-to-side anastomosis. For a discussion and a comparative approach see, for example, Cole et al. [11]. Bypass can be made by organic material (e.g. the saphena vein taken from patients legs or the mammary artery) or by prosthetic material.

The graft patency affects the long-term efficacy of coronary bypass procedures, and several post-surgical complications have to be taken into consideration. Among them, we mention intimal thickening hyperplasia (near suture lines), which is a narrowing of coronary arteries, restenosis,

DOI: 10.1002/fld

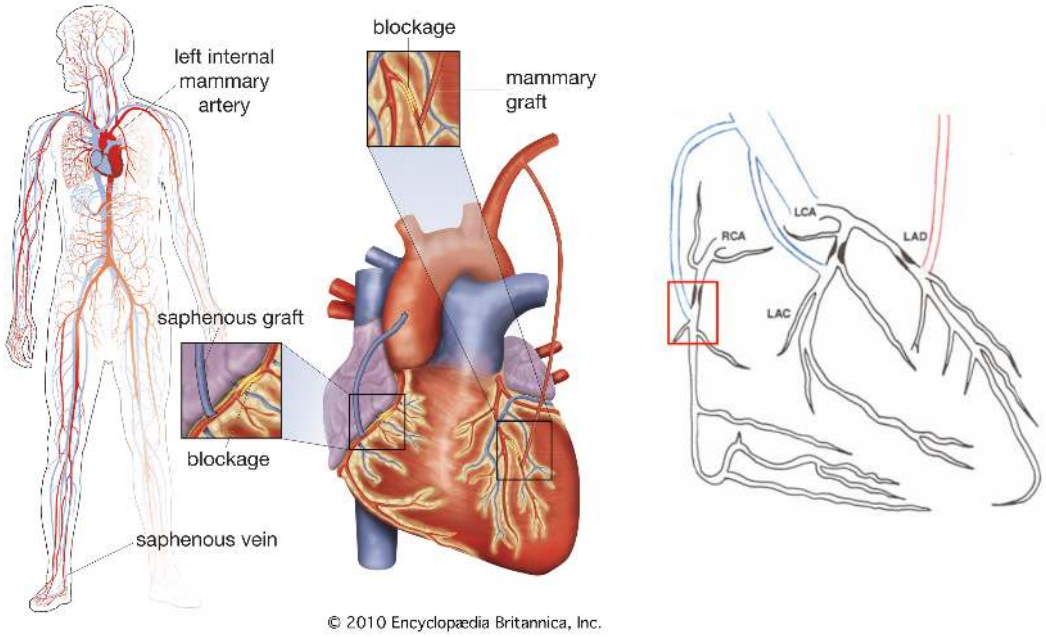

Figure 14. Left: double coronary artery bypass surgery, showing the grafting of a section of saphenous vein from the leg to bypass a blockage on the right side of the heart and the diversion of an internal mammary artery to bypass a blockage on the left side of the heart (picture taken from Encyclopædia Britannica, Inc.). Right: coronary tree and possible end-to-side aorto-coronary bypasses.

surgical injury, long term graft failure[e]. One of the most important process is atherosclerotic obstruction occurring on a foundation of neointimal hyperplasia. This thickening, which results from an accumulation of muscle cells and extracellular matrix in the intimal compartment, is the principal disease process in venous bypass grafting during the first post-surgical year and represents the foundation for later development of graft atheroma and atheromatous plaques.

Computational fluid dynamics (CFD) helps understanding local haemodynamics phenomena and the effect of vascular wall modication on flow patterns (e.g. [13, 26]). This can have useful clinical applications especially in surgical procedures. Moreover, computational studies have highlighted the correlation between geometrical features (such as anastomotic angle and graft-artery diameter ratio) and vorticity, shear stress, shear stress gradient [25, 45] and oscillatory shear index [34], as effect of recirculation, flow separation and moving stagnation zones [11, 14].

For the problem at hand, we are interested in the minimization of the blood vorticity in the down-field region of the bypass by changing the shape of the anastomosis. In fact, high vorticity areas are responsible of atherogenesis or intimal hyperplasia, which can eventually lead to the failure of grafting surgery.

[e] In particular, during the first year after bypass surgery up to 15% of venous graft occlude, while by ten years after only 60% of vein grafts are patent and only 50% of patent vein grafts are free of significant stenosis [14, 30]. Moreover, every year 8% of all patients risk bypass occlusion, after ten years 80% bypasses must be replaced.

DOI: 10.1002/fld

ACKNOWLEDGEMENTS

We acknowledge the use of `MLife` library previously developed by Prof. Fausto Saleri as a basis for the numerical FE simulations presented in this paper. We also acknowledge, in the framework of the Progetto Roberto Rocca (MIT-Politecnico di Milano), Prof. A.T. Patera (MIT) for his insights on treatment of noncoercive problems, as well as all the people who have contributed with him to the `rbMIT` package used for RB computations presented in this work. In particular, we thank Dr. P. Huynh (MIT) and Dr. T. Lassila (Aalto University) for their feedbacks and suggestions.
This work has been supported in part by the Swiss National Science Foundation (Project 200021-122136) and by the ERC-Mathcard Project (Project ERC-2008-AdG 227058).

REFERENCES

1. V. Agoshkov, A. Quarteroni, and G. Rozza. Shape design in aorto-coronaric bypass anastomoses using perturbation theory. *SIAM J. Numer. Anal.*, 44(1):367–384, 2006.
2. G. Allaire. *Conception optimale de structures*. Springer, vol. 58 Mathématiques et Applications, 2007.
3. E.I. Amoiralis and I.K. Nikolos. Freeform deformation versus B-spline representation in inverse airfoil design. *Journal of Computing and Information Science in Engineering*, 8(2), 2008.
4. M. Barrault, Y. Maday, N.C. Nguyen, and A.T. Patera. An 'empirical interpolation' method: application to efficient reduced-basis discretization of partial differential equations. *C.R. Math. Acad. Sci. Paris, Series I*, 339(9):667–672, 2004.
5. F. Bélahcène and J.A. Désidéri. Paramétrisation de Bézier adaptative pour l'optimisation de forme en Aérodynamique. *INRIA, Rapp. de rech. no. 4943*, 2003.
6. M. Berggren. Numerical solution of a flow-control problem: vorticity reduction by dynamic boundary action. *SIAM J. Sci. Comput.*, 19(3):829–860, 1998.
7. M. Botsch and I. Kobbelt. Freeform shape representations for efficient geometry processing. *International Conference on Shape Modeling and Applications*, 2003.
8. J. Cea. Conception optimale ou identification de formes: calcul rapide de la dérivée directionelle de la fonction cout. *Mathematical Modelling and Numerical Analysis*, 20(3):371–402, 1986.
9. J. Céa, S. Garreau, P. Guillaume, and M. Masmoudi. The shape and topological optimizations connection. *Computer Methods in Applied Mechanics and Engineering*, 188:713–726, 2000.
10. A. Clarich and J.A. Désidéri. Self-adaptive parametrisation for aerodynamic optimum-shape design. *INRIA, Rapp. de rech. no. 4428*, 2002.
11. J. Cole, J. Watterson, and M. O'Reilly. Numerical investigation of the haemodynamics at a patched arterial bypass anastomosis. *Medical Engineering & Physics*, 24:393–401, 2002.
12. L. Dedè. *Adaptive and reduced basis methods for optimal control problems in environmental applications*. PhD thesis, Politecnico di Milano, 2008. Available at `http://mox.polimi.it`.
13. L. Formaggia, A. Quarteroni, and A. Veneziani. *Cardiovascular Mathematics. Modeling and simulation of the circulatory system*. Springer, Series MS&A, Vol. 1, 2009.
14. T. Frauenfelder, E. Boutsianis, T. Schertler, L. Husmann, S. Leschka, D. Poulikakos, B. Marincek, and H. Alkadhi. Flow and wall shear stress in end-to-side and side-to-side anastomosis of venous coronary artery bypass grafts. *BioMedical Engineering OnLine*, 35(6), 2007.
15. M. Grepl, Y. Maday, N.C. Nguyen, and A.T. Patera. Efficient reduced-basis treatment of nonaffine and nonlinear partial differential equations. *ESAIM Math. Modelling Numer. Anal.*, 41(3):575–605, 2007.
16. M.D. Gunzburger. *Perspectives in Flow Control and Optimization*. SIAM, 2003.
17. M.D. Gunzburger, H. Kim, and S. Manservisi. On a shape control problem for the stationary Navier-Stokes equations. *Mathematical Modelling and Numerical Analysis*, 34(6):1233–1258, 2000.
18. J. Haslinger and R.A.E. Mäkinen. *Introduction to shape optimization: theory, approximation, and computation*. SIAM, 2003.
19. A. Henrot and M. Pierre. *Variation et optimisation de formes. Une analyse géométrique*. Springer, Series Mathématiques et Applications, Vol. 48, 2005.

DOI: 10.1002/fld

20. M. Hinze, R. Pinnau, M. Ulbrich, and S. Ulbrich. *Optimization with PDE Constraints*. Springer, Series Mathematical Modelling: Theory and Applications, Vol. 23, 2009.
21. P. Huynh, N.C. Nguyen, G. Rozza, and A.T. Patera. Rapid reliable solution of the parametrized partial differential equations of continuum mechanics and transport, 2008-2010. `http://augustine.mit.edu`.
22. P. Huynh, G. Rozza, S. Sen, and A.T. Patera. A successive constraint linear optimization method for lower bounds of parametric coercivity and inf-sup stability costants. *C. R. Acad. Sci. Paris, Series I*, 345:473–478, 2007.
23. T. Lassila and G. Rozza. Parametric free-form shape design with PDE models and reduced basis method. *Comput. Meth. Appl. Mech. Engr.*, 199:1583–1592, 2010.
24. T. Lehnhäuser and M. Schäfer. A numerical approach for shape optimization of fluid flow domains. *Comput. Methods Appl. Mech. Engrg.*, 194:5221–5241, 2005.
25. M. Lei, J. Archie, and C. Kleinstreuer. Computational design of a bypass graft that minimizes wall shear stress gradients in the region of the distal anastomosis. *Journal of Vascular Surgery*, 25(4):637–646, 1997.
26. F. Loth, P.F. Fischer, and H.S. Bassiouny. Blood flow in end-to-side anastomoses. *Annu. Rev. Fluid. Mech.*, 40:367–393, 2008.
27. B. Mohammadi and O. Pironneau. *Applied shape optimization for fluids*. Oxford University Press, 2001.
28. N. C. Nguyen, K. Veroy, and A. T. Patera. Certified real-time solution of parametrized partial differential equations. In S. Yip, editor, *Handbook of Materials Modeling*, pages 1523–1558. Springer, 2005.
29. N.C. Nguyen. A posteriori error estimation and basis adaptivity for reduced-basis approximation of nonaffine-parametrized linear elliptic partial differential equations. *J. Comp. Phys.*, 227:983–1006, 2007.
30. P. Parang and R. Arora. Coronary vein graft disease: Pathogenesis and prevention. *Can J Cardiol*, 25(2):e57–e62, 2009.
31. A.T. Patera and G. Rozza. *Reduced Basis Approximation and A Posteriori Error Estimation for Parametrized Partial Differential Equations*. Version 1.0, 2006, Copyright MIT, to appear in (tentative rubric) MIT Pappalardo Graduate Monographs in Mechanical Engineering. Available at `http://augustine.mit.edu`.
32. A. Quarteroni. *Numerical Models for Differential Problems*. Springer, Series MS&A, Vol. 2, 2009.
33. A. Quarteroni and G. Rozza. Optimal control and shape optimization of aorto-coronaric bypass anastomoses. *Math. Models Meth. Appl. Sci.*, 13(12):1801–1823, 2003.
34. G. Rozza. *Shape design by optimal flow control and reduced basis techniques: applications to bypass configurations in haemodynamics*. PhD thesis, N. 3400, École Polytechnique Fédérale de Lausanne, 2005. Available at `http://library.epfl.ch/en/theses/?nr=3400`.
35. G. Rozza. Reduced basis methods for Stokes equations in domains with non-affine parameter dependence. *Comput. Vis. Sci.*, 12(1):23–35, 2009.
36. G. Rozza, P. Huynh, and A. Manzoni. Reduced basis approximation and error bounds for Stokes flows in parametrized geometries: roles of the inf-sup stability constants. *MATHICSE Report 22.2010. Submitted*, 2010. Available at `http://infoscience.epfl.ch`.
37. G. Rozza, P. Huynh, and A.T. Patera. Reduced basis approximation and a posteriori error estimation for affinely parametrized elliptic coercive partial differential equations. *Arch. Comput. Methods Engrg.*, 15:229–275, 2008.
38. G. Rozza, T. Lassila, and A. Manzoni. Reduced basis approximation for shape optimization in thermal flows with a parametrized polynomial geometric map. In *Spectral and High Order Methods for Partial Differential Equations. Selected papers from the ICOSAHOM '09 conference, June 22-26, Trondheim, Norway*, pages 307–315. Springer, Series: Lecture Notes in Computational Science and Engineering, vol. 76, J.S. Hesthaven, E.M. Rønquist (Eds.), 2011.
39. G. Rozza and A. Manzoni. Model order reduction by geometrical parametrization for shape optimization in computational fluid dynamics. In *Proceedings of ECCOMAS CFD 2010, V European Conference on Computational Fluid Dynamics, Lisbon, Portugal, J.C.F. Pereira and A. Sequeira (Eds.)*, 2010.
40. G. Rozza and K. Veroy. On the stability of the reduced basis method for Stokes equations in parametrized domains. *Comput. Meth. Appl. Mech. Engr.*, 196(7):1244–1260, 2007.
41. F. Saleri, P. Gervasio, G. Rozza, and A. Manzoni. `MLIfe`, A Matlab LIbrary for Finite Elements, tutorial (in progress). *MOX, Politecnico di Milano and CMCS, Ecole Polytechnique Fédérale de Lausanne*, 2000–2010. ©Politecnico di Milano.
42. T.W. Sederberg and S.R. Parry. Free-form deformation of solid geometric models. *Comput. Graph.*, 20(4):151–160, 1986.
43. J. Sokolowski and J.-P. Zolésio. *Introduction to shape optimization: shape sensitivity analysis*. Springer-Verlag, 1992.
44. J.R. Womersley. Method for the calculation of velocity, rate flow, and viscous drag in arteries when the pressure gradient is known. *J. Physiol.*, 127(3):553–563, 1955.

DOI: 10.1002/fld

45. F. Xiong and C. Chong. A parametric numerical investigation on haemodynamics in distal coronary anastomoses. *Medical Engineering & Physics*, 30(3):311–320, 2008.

DOI: 10.1002/fld